



CLASSY. IX. The Chemical Evolution of the Ne, S, Cl, and Ar Elements

Karla Z. Arellano-Córdova^{1,2} , Danielle A. Berg² , Matilde Mingozzi³ , Bethan L. James³ , Noah S. J. Rogers⁴ , Evan D. Skillman⁵ , Fergus Cullen¹ , Ryan K. Alexander^{6,7,8} , Ricardo O. Amorín^{9,10} , John Chisholm² , Matthew Hayes¹¹ , Timothy Heckman¹² , Svea Hernandez³ , Nimisha Kumari³ , Claus Leitherer¹³ , Crystal L. Martin¹⁴ , Michael Maseda¹⁵ , Themiyi Nanayakkara¹⁶ , Kaelee Parker², Swara Ravindranath^{17,18} , Allison L. Strom¹⁹ , Fiorenzo Vincenzo^{6,7} , and Aida Wofford^{20,21}

¹ Institute for Astronomy, University of Edinburgh, Royal Observatory, Edinburgh, EH9 3HJ, UK; ziboney@gmail.com, k.arellano@ed.ac.uk

² Department of Astronomy, The University of Texas at Austin, 2515 Speedway, Stop C1400, Austin, TX 78712, USA

³ AURA for ESA, Space Telescope Science Institute, 3700 San Martin Drive, Baltimore, MD 21218, USA

⁴ Center for Interdisciplinary Exploration and Research in Astrophysics (CIERA), Northwestern University, 1800 Sherman Avenue, Evanston, IL 60201, USA

⁵ Minnesota Institute for Astrophysics, University of Minnesota, 116 Church Street SE, Minneapolis, MN 55455, USA

⁶ E.A. Milne Centre for Astrophysics, University of Hull, Hull, HU6 7RX, UK

⁷ Joint Institute for Nuclear Astrophysics, Center for the Evolution of the Elements (JINA-CEE), 640 S Shaw Lane, East Lansing, MI 48824, USA

⁸ Centre of Excellence for Data Science, AI, and Modelling (DAIM), University of Hull, Cottingham Road, Kingston-upon-Hull, HU6 7RX, UK

⁹ ARAID Foundation, Centro de Estudios de Física del Cosmos de Aragón (CEFCA), Unidad Asociada al CSIC, Plaza San Juan 1, E-44001 Teruel, Spain

¹⁰ Departamento de Astronomía, Universidad de La Serena, Av. Juan Cisternas 1200 Norte, La Serena 1720236, Chile

¹¹ Stockholm University, Department of Astronomy and Oskar Klein Centre for Cosmoparticle Physics, AlbaNova University Centre, SE-10691, Stockholm, Sweden

¹² Center for Astrophysical Sciences, Department of Physics & Astronomy, Johns Hopkins University, Baltimore, MD 21218, USA

¹³ Space Telescope Science Institute, 3700 San Martin Drive, Baltimore, MD 21218, USA

¹⁴ Department of Physics, University of California, Santa Barbara, Santa Barbara, CA 93106, USA

¹⁵ Department of Astronomy, University of Wisconsin-Madison, Madison, WI 53706, USA

¹⁶ Swinburne University of Technology, Melbourne, Victoria, Australia

¹⁷ Astrophysics Science Division, NASA Goddard Space Flight Center, 8800 Greenbelt Road, Greenbelt, MD 20771, USA

¹⁸ Center for Research and Exploration in Space Science and Technology II, Department of Physics, Catholic University of America, 620 Michigan Avenue N.E., Washington, DC 20064, USA

¹⁹ Department of Astrophysical Sciences, Princeton University, 4 Ivy Lane, Princeton, NJ 08544, USA

²⁰ Instituto de Astronomía, Universidad Nacional Autónoma de México, Unidad Académica en Ensenada, Km 103 Carr. Tijuana-Ensenada, Ensenada 22860, México

²¹ Department of Astronomy & Astrophysics, University of California San Diego, 9500 Gilman Drive, La Jolla, CA 92093, USA

Received 2024 January 18; revised 2024 March 12; accepted 2024 March 13; published 2024 June 14

Abstract

To study the chemical evolution across cosmic epochs, we investigate Ne, S, Cl, and Ar abundance patterns in the Cosmic Origins Spectrograph Legacy Archive Spectroscopic Survey (CLASSY). CLASSY comprises local star-forming galaxies (SFGs; $0.02 < z < 0.18$) with enhanced star formation rates, making them strong analogues to high- z SFGs. With direct measurements of electron temperature, we derive accurate ionic abundances for all elements and assess ionization correction factors (ICFs) to account for unseen ions and derive total abundances. We find Ne/O, S/O, Cl/O, and Ar/O exhibit constant trends with gas-phase metallicity for $12 + \log(\text{O}/\text{H}) < 8.5$ but significant correlation for Ne/O and Ar/O with metallicity for $12 + \log(\text{O}/\text{H}) > 8.5$, likely due to ICFs. Thus, the applicability of the ICFs to integrated spectra of galaxies could bias results, underestimating true abundance ratios. Using CLASSY as a local reference, we assess the evolution of Ne/O, S/O, and Ar/O in galaxies at $z > 3$, finding no cosmic evolution of Ne/O, while the lack of direct abundance determinations for S/O and Ar/O can bias the interpretation of the evolution of these elements. We determine the fundamental metallicity relationship (FMR) for CLASSY and compare to the high-redshift FMR, finding no evolution. Finally, we perform the first mass–neon relationship analysis across cosmic epochs, finding a slight evolution to high Ne at later epochs. The robust abundance patterns of CLASSY galaxies and their broad range of physical properties provide essential benchmarks for interpreting the chemical enrichment of the early galaxies observed with the JWST.

Unified Astronomy Thesaurus concepts: Galaxy abundances (574); Dwarf galaxies (416); H II regions (694); Gaseous nebulae (639); High-redshift galaxies (734); Compact dwarf galaxies (281)

1. Introduction

Recent observations of JWST have opened a new window into the exploration of the chemical enrichment of galaxies at $z > 6$ (e.g., Arellano-Córdova et al. 2022a; Schaerer et al. 2022; Brinchmann 2023; Curti et al. 2023; Isobe et al. 2023b; Nakajima et al. 2023; Rhoads et al. 2023). The determination of the oxygen abundances (O/H, often referred to as metallicity)

is an essential goal of JWST observations due to its strong relationship with galaxy properties such as stellar mass and star formation rate (SFR). Such scaling relationships involve diverse mechanisms associated with galaxy formation and evolution such as star formation, outflows, or inflows of pristine gas (i.e., the baryon cycle; Tremonti et al. 2004; Tumlinson et al. 2017). Impressively, direct O/H abundances have already been computed for a small number of sources thanks to the successful detection of the temperature-sensitive emission line of [O III] $\lambda 4363$ at $z > 7$ (e.g., Arellano-Córdova et al. 2022a; Schaerer et al. 2022; Curti et al. 2023; Rhoads et al. 2023; Trump et al. 2023; Laseter et al. 2024). While direct

abundance determinations are often viewed as the most robust method, recent temperature inhomogeneities results in H II regions may result in a strong bias in objects with a high degree of ionization, like those observed at $z < 7$ (Arellano-Córdova et al. 2022a; Méndez-Delgado et al. 2023a; Cameron et al. 2024a). Such bias might have a significant impact on important scaling relations such as the mass–metallicity relation (MZR) in metal-poor objects. Samples of galaxies at $z \sim 0$ with robust determinations of electron temperature (i.e., T_e , using different line diagnostics) and metallicities are crucial to assess this bias and the potential impacts on high-redshift abundance determinations.

In addition to oxygen, strong emission lines associated with other elements are now being clearly detected at $z > 4$ (e.g., Arellano-Córdova et al. 2022a; Isobe et al. 2023b; Jones et al. 2023; Nakajima et al. 2023; Marques-Chaves et al. 2024). An example includes Ne, S, and Ar, which are the most typical α -elements observed in nebular studies in the local Universe (Izotov et al. 2006; Croxall et al. 2016). We do not include nitrogen here because it is the focus of an upcoming paper (K. Z. Arellano-Córdova et al. 2024, in preparation; see also, Stephenson et al. 2023). These elements are ejected into the interstellar medium by core-collapse supernovae (CCSNe; Henry & Worthey 1999; Kobayashi et al. 2020a; Prantzos et al. 2020).

Before JWST, the majority of α -element abundance measurements were limited to H II regions and star-forming galaxies (SFGs) from the local Universe (e.g., Izotov et al. 2006, 2011; Guseva et al. 2011; Gusev et al. 2012; Croxall et al. 2016; Berg et al. 2018, 2019; Kumari et al. 2019; Arellano-Córdova et al. 2020; Díaz & Zamora 2022; Domínguez-Guzmán et al. 2022; Rogers et al. 2022). In general, many studies report little-to-no variation between α -elements with respect to O and metallicity (e.g., Kennicutt et al. 2003a; Izotov et al. 2006; Berg et al. 2021; Rogers et al. 2022), with the exception of S/O, which has been seen to decrease significantly as metallicity increases (e.g., S/O versus O/H, Izotov et al. 2006; Guseva et al. 2011; Amayo et al. 2021; Díaz & Zamora 2022).

Recent observations with JWST now present the opportunity to determine the chemical abundances of galaxies at high- z . Chemical abundances of SFGs have been studied in surveys like CEERS, GLASS, and JADES (Treu et al. 2022; Finkelstein et al. 2023; Eisenstein et al. 2024). For example, the abundance ratio of C/O has been reported in a few galaxies at $z > 6$ (e.g., Jones et al. 2012; Arellano-Córdova et al. 2022a; Cameron et al. 2023b; Marques-Chaves et al. 2024), while the chemical abundances of Ne, S, and Ar have been determined for multiple SFGs at $z = 4\text{--}8$ (e.g., Isobe et al. 2023a). Arellano-Córdova et al. (2022a) reported Ne/O abundance ratios for three galaxies at $z > 7$ using spectra from the JWST Early Release Observations (ERO; Pontoppidan et al. 2022). Comparing their results with local SFGs, the authors found that Ne/O does not appear to evolve with redshift. In the recent work by Isobe et al. (2023b), they studied the Ne/O ratio for a large sample of SFGs at $z \sim 4\text{--}10$ in comparison with chemical evolution models (Watanabe et al. 2024). These authors also found comparable results to those observed in galaxies at $z \sim 0$ (Izotov et al. 2006; Arellano-Córdova et al. 2022b; Isobe et al. 2022, e.g.).

Unfortunately, being unable to estimate T_e in most of the high- z galaxies in Isobe et al. (2023b) makes it hard to interpret

the redshift evolution of Ne, S, and Ar. In general, accurate determinations of chemical abundances (e.g., C, N, Ne, S, Cl, Ar, and Fe) rely on two key aspects, (1) the robust measurement of T_e (and electron density; see also, Sanders et al. 2016; Isobe et al. 2023a; Méndez-Delgado et al. 2023b) and (2) accurate ionization correction factors (ICFs; essential to account for the unseen ions; e.g., Peimbert & Costero 1969; Thuan et al. 1995; Izotov et al. 2006; Pérez-Montero et al. 2007; Dors et al. 2016; Peimbert et al. 2017; Amayo et al. 2021; Berg et al. 2021).

The nebular structures are complex in nature; the issue here is that the integrated observations do not capture this complexity. In principle, ICFs are constructed under the prescription of a single ionization source or H II region, resulting in a potentially large bias when these are applied to the integrated spectra of SFGs. This could result in spurious trends that are not compatible with the prediction of chemical evolution models (e.g., Alexander et al. 2023; Watanabe et al. 2024), and in turn, bias our interpretation of the abundance patterns in the early Universe. Therefore, to decipher the chemical evolution of these elements, it is more important than ever to establish samples of nearby galaxies that span an ample range of conditions in order to correctly understand physical properties of galaxies at high- z . Local SFGs allow us to disentangle the ionization and temperature structure (Izotov et al. 2006, 2012; Guseva et al. 2012; Arellano-Córdova et al. 2022a; Mingozzi et al. 2024, hereafter Paper IV). Thus, they provide a robust path to generate tools to understand the abundance ratios of metals from $z \sim 0$ to $z > 4$ in galaxies already observed with the JWST such as CECILIA (Strom et al. 2023), and enable us to be prepared for the upcoming observations of the Extremely Large Telescopes.

The main aim of this paper is to study the chemical evolution of Ne, S, Cl, and Ar.²² These elements are synthesized in the interiors of massive stars as O. Therefore, their study can help us to constrain chemical evolution models of galaxies, particularly, to compare observations of SFGs at different redshifts with theoretical models to understand the role of the CCSNe yields, which still suffer from large uncertainties. In this context, we use a sample of local SFGs from the Cosmic Origins Spectrograph (COS) Legacy Archive Spectroscopic Survey (CLASSY; Berg et al. 2022, hereafter Paper I; James et al. 2022) with properties similar to high- z galaxies (stellar mass, SFR, and ionization parameter) characterizing robustly their physical conditions and ionic abundances. With CLASSY, we can inspect the ICFs to provide information concerning the potential biases affecting the computation of total abundance ratios. The analysis of the CLASSY galaxies will be a robust template to interpret the chemical evolution of metals across cosmic time.

The structure of this paper is as follows: In Section 2, we present the sample used in this analysis. Section 3 describes the methodology utilized to derive the physical condition and ionic abundances. The analysis of the ICFs and the total abundances is also described. The results for the abundance patterns of CLASSY are presented in Section 4.2. In Section 5, we compare our results with the abundance patterns of high- z galaxies and the bias in abundance determinations at high- z . In Section 6, we also discuss the evolution of some scaling relations. In Section 7, we summarize our conclusions.

²² N/O and C/O abundances will be presented in upcoming CLASSY papers.

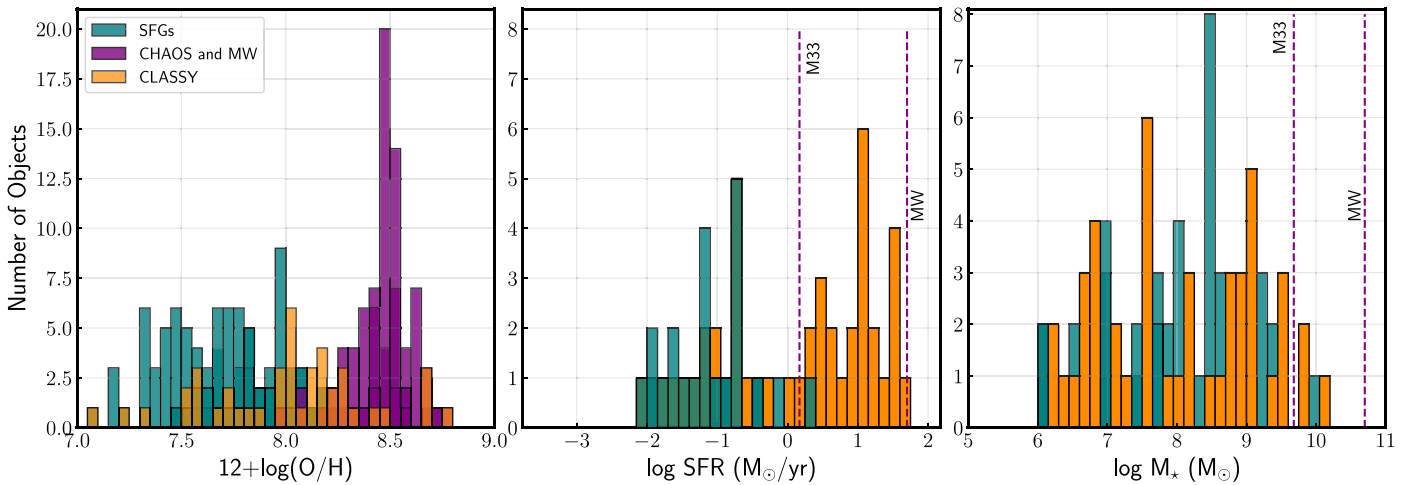


Figure 1. Metallicity, SFR, and stellar mass of the CLASSY sample in comparison to the additional sample of SFGs and H II regions collected from literature (Berg et al. 2012, 2016, 2019; Izotov et al. 2012, 2017; Croxall et al. 2016; Arellano-Córdova et al. 2020, 2021; Rogers et al. 2022). The dashed lines identify the range in SFR and stellar mass of the M33 galaxy, and the Milky Way (MW) taken from Elia et al. (2022), Williams et al. (2018), Berg et al. (2020), and Licquia & Newman (2015), respectively.

In this paper, we use the following solar abundance ratios taken from Asplund et al. (2021): $\text{Ne}/\text{O}_{\odot} = -0.63 \pm 0.06$, $\text{S}/\text{O}_{\odot} = -1.57 \pm 0.05$, $\text{Cl}/\text{O}_{\odot} = -3.38 \pm 0.20$, and $\text{Ar}/\text{O}_{\odot} = -2.31 \pm 0.11$ with a solar oxygen abundance of $12+\log(\text{O}/\text{H}) = 8.69 \pm 0.04$.

2. Sample

2.1. Main Sample

We use the ancillary optical spectra of 43 local ($0.002 < z < 0.18$) SFGs from CLASSY (James et al. 2022; Paper I). This collection of optical spectra comprises observations from the Astrophysical Observatory of the Smithsonian Institution/SDSS, the Large Binocular Telescope (LBT)/MODS, Very Large Telescope/MUSE/VIMOS, and MMT telescopes/instruments, with a broad range of physical properties (see Figure 1) such as reddening ($0.02 < E(B-V) < 0.67$), electron density, ($10 < n_e \text{ (cm}^{-3}\text{)} < 1120$), metallicity ($7.0 < 12+\log(\text{O}/\text{H}) < 8.7$), a proxy of the ionization degree ($0.5 < [\text{O III}] \lambda 5007/[\text{O II}] \lambda 3727 < 38.0$), stellar mass ($6.2 < \log(M_{*}/M_{\odot}) < 10.1$), and SFR ($-2.0 < \log \text{SFR} (M_{\odot} \text{ yr}^{-1}) < +1.6$). The details concerning the optical observation are reported in Paper I, Paper IV, and Arellano-Córdova et al. (2022b, hereafter Paper V).

2.2. Comparison Samples

In addition, we have compiled different samples of SFGs and H II regions of disk galaxies to compare with the results of the abundance patterns of CLASSY. For this additional sample, it was also possible to derive the chemical abundances using the measurements of electron temperature.

Integrated SFGs. We selected a sample of local dwarf SFGs reported in Berg et al. (2012, 2016), Izotov et al. (2006, 2012, 2017), and Berg et al. (2019). We selected this sample because it covers lower metallicities ($7.0 < 12+\log(\text{O}/\text{H}) < 8.2$), and the abundances are based on the T_e -sensitive method. Therefore, this sample will be useful to compare with our results for CLASSY.

H II regions. We have selected 44 Galactic H II regions of Arellano-Córdova et al. (2020, 2021) with measurements of C, N, O, S, Cl, and Ar. This sample of Galactic H II regions covers a range in metallicity of $8.0 < 12+\log(\text{O}/\text{H}) < 8.9$. In addition, we use H II regions from The Chemical Abundances

Of Spirals (CHAOS) project, which comprises ~ 200 H II regions with chemical abundance determinations using the robust measurements of electron temperature (Croxall et al. 2016; Berg et al. 2020; Rogers et al. 2021, 2022). We have selected those H II regions reported in the M33 galaxy (Rogers et al. 2022), which cover a range in metallicity between $8.0 < 12+\log(\text{O}/\text{H}) < 8.7$. The chemical abundances of CHAOS were derived following a methodology similar to this work as we explain below.

3. Nebular Physical Conditions

To analyze the nebular gas of the CLASSY sample, we utilized the nebular analysis package PyNeb (Luridiana et al. 2015, version 1.1.14) to calculate the electron density (n_e) and (T_e) and chemical abundances. The physical conditions are based on our selection of atomic data using the five-level atom model (De Robertis et al. 1987). The atomic data used in this study are listed in Table 1.

We determine the physical conditions and chemical abundances for all samples using a uniform method consistent with the procedure utilized for CLASSY. We use the reddening corrected fluxes compiled from SFGs reported in Berg et al. (2016, 2019), Izotov et al. (2006, 2017, 2021). While for the sample of H II regions (CHAOS and the Milky Way H II regions), we have taken the chemical abundances reported in the original papers. In Figure 1, we show the range in metallicity (left), SFR (middle), and stellar mass (right) covered by the CLASSY sample and the additional sample.

T_e and n_e are key to deriving accurate chemical abundances. In particular, it requires the detection of faint emission features sensitive to the electron temperature such as the $[\text{O III}] \lambda 4363$, $[\text{N II}] \lambda 5755$, $[\text{S III}] \lambda 6312$, and $[\text{O II}] \lambda \lambda 7320, 7330$ auroral lines. Fortunately, in most of the CLASSY sample, we detect at least one T_e -sensitive line, and for others, it is possible to trace the temperature structure using T_e -diagnostics (see Paper I and Paper IV). In Paper I, we have also identified those T_e diagnostics used in the determination of the metallicity. For those galaxies with higher metallicity, we also inspected the $[\text{O III}] \lambda 4363$ profile to avoid any contamination of $[\text{Fe II}] \lambda 4359$ (Curti et al. 2017; $12+\log(\text{O}/\text{H}) > 8.4$) to the observed

Table 1
Atomic Data Used in This Work

Ion	Transition Probabilities	A_{ij}^a	Collision Strengths	Υ_{ij}^a
O ⁺	Froese Fischer & Tachiev (2004)	FFT04	Kisielius et al. (2009)	Kal09
O ²⁺	Froese Fischer & Tachiev (2004)	FFT04	Aggarwal & Keenan (1999)	AK99
N ⁺	Froese Fischer & Tachiev (2004)	FFT04	Tayal (2011)	T11
Ne ²⁺	McLaughlin et al. (2011)	McL11	McLaughlin et al. (2011)	McL11
S ⁺	Podobedova et al. (2009)	PKW09	Tayal & Zatsarinny (2010)	TZ10
S ²⁺	Podobedova et al. (2009)	PKW09	Grieve et al. (2014)	GRHK14
Cl ²⁺	Fritzsche et al. (1999)	Fal99	Butler & Zeppen (1989)	BZ89
Cl ³⁺	Kaufman & Sugar (1986), Mendoza & Zeppen (1982a), Ellis & Martinson (1984)	KS86-MZ82-EM84	Galavis et al. (1995)	GMZ95
Ar ²⁺	Mendoza (1983), Kaufman & Sugar (1986)	M83-KS86	Galavis et al. (1995)	GMZ95
Ar ³⁺	Mendoza & Zeppen (1982b)	MZ82	Ramsbottom & Bell (1997)	RB97

Note.

^a Identified as in PYNEB: Υ_{ij_coll} (Collision Strengths) and “ A_{ij_atom} , (Transition Probabilities)” respectively.

flux of [O III] $\lambda 4363$, implying an underestimate of T_e [O III] (see also Paper IV; Arellano-Córdova & Rodríguez 2020).

3.1. n_e Measurements

n_e was calculated for the CLASSY galaxies using the [S II] $\lambda 6731/\lambda 6717$ diagnostic ratio, which primarily traces the low-ionization region of the gas. A detailed analysis of different density diagnostics is presented in Paper IV, which shows no significant differences in the metallicities calculated using other density diagnostics. Abundances are insensitive to densities below $n_e \sim 5000 \text{ cm}^{-3}$ for $12+\log(\text{O}/\text{H})$ (<0.2 dex difference than the low density limit), and are insensitive to even higher densities for other ratios like Ne/O and Ar/O (Osterbrock & Ferland 2006).

Density uncertainties were determined using a bootstrap Monte Carlo error analysis. For each galaxy, we generated 1000 mock densities calculated by sampling [S II] ratios from a Gaussian distribution centered at the observed intensity ratio and with a width equal to the ratio uncertainty. The standard deviation of the 1000 simulated densities was then taken as the uncertainty on the calculated density.

3.2. T_e Measurements

We compute the electron temperature for the CLASSY galaxies with the following T_e -diagnostic ratios: [O II] $\lambda\lambda 3726, 3729/(\lambda\lambda 7319, 7320 + \lambda\lambda 7330, 7331)$,²³ [N II] $\lambda\lambda 6548, 6584/\lambda 5755$, [S III] $\lambda\lambda 9069, 9532/\lambda 6312$, and [O III] $\lambda\lambda 4959, 5007/\lambda 4363$, for the low- T_e [O II] (or $-T_e$ [N II]), intermediate- T_e [S III], and high- T_e [O III] ionization temperatures, respectively. It is important to mention that the [S III] lines can be strongly contaminated by telluric absorption in ground-based spectra, which is difficult to assess without the detection of [S III] $\lambda 9532$, which is typically more strongly affected (Vacca et al. 2003), especially in $z = 0$ objects. For most of the spectra, it was only possible to measure [S III] $\lambda 9069$. We have used it with the [S III] theoretical emissivity ratio to estimate the intensity of [S III] $\lambda 9532$ ([S III] $\lambda 9532/\lambda 9069 = 2.47$). In Table 5, in Appendix C, we list the results for n_e and T_e associated with the different diagnostics used in columns (2)–(6). These temperatures represent different ionization regions of the galaxy (see also Paper IV).

Only one or two T_e -diagnostics were available for each galaxy. These diagnostics trace different regions of the gas based on the ionization structure of the nebula. If only one of T_e -diagnostics is available, T_e - T_e relations are used to estimate the unavailable T_e for a specific ionization region. To determine the complete temperature structure of each region, we have assessed some temperature relations from the literature (e.g., Garnett 1990; Izotov et al. 2006) using CLASSY. We inspected such temperature relations minimize the uncertainties on the estimate of the missing temperature. In Appendix A, we compare several theoretical and empirical T_e - T_e relationships and find that the relationships of Garnett (1992) work well to estimate T_e (Low) and T_e (Int.) from T_e [O III]. Additionally, we adopt the relationships of Rogers et al. (2021) when T_e [O III] is not measured. In Appendix Table 5, we present the results for T_e (Low), T_e (Int.), and T_e (High) in columns (7)–(9), which represents the temperature structure for the CLASSY sample in this paper.

To calculate the uncertainties associated with the electron temperatures and density, we use Monte Carlo simulations. We generated a Gaussian distribution of 1000 random values for each line intensity of each galaxy. The distribution was centered at the observed intensity, with a σ equal to the associated uncertainty derived using standard deviation.

4. Nebular Abundances

We use the following equation to calculate ionic abundances relative to hydrogen:

$$\frac{N(X^i)}{N(H^+)} = \frac{I_{\lambda(X^i)} j_{H\beta}}{I_{H\beta} j_{\lambda(X^i)}}, \quad (1)$$

where $j_{\lambda(X^i)}$, the emissivity coefficient, is sensitive to the adopted temperature. We derive the ionic abundances of O, Ne, S, Cl, and Ar, using the three-zone temperature structure adopted in Section 3 (T_e (Low), T_e (Int), and T_e (High)). We use T_e (Low) to calculate the ionic abundances of the low-ionization ions such as O⁺ and S⁺. For O⁺, we use the measurements of [O II] $\lambda 3727$ when available and [O II] $\lambda\lambda 7320, 7330$ lines for the rest of the galaxies. For S⁺, we use the measurements of [S II] $\lambda\lambda 6717, 6731$ lines, respectively. To calculate the ionic abundances of intermediate ionization ions, S²⁺, Cl²⁺, and Ar²⁺, we use the measurements of [S III] $\lambda 6312, 9069$, [Cl III] $\lambda 5518, 5538$, and [Ar III] $\lambda 7135, 7751$ lines, and T_e (Int) as a

²³ Hereafter referred to as [O II] $\lambda 3727$ and [O II] $\lambda\lambda 7320, 7330$ since such lines are blended due to the spectral resolution of the sample.

representative temperature of the intermediate ionization zone. For S, we have determined the S^{2+} using [S III] $\lambda 6312$, which allows us to increase the number of galaxies with measurements of S^{2+} . Therefore, for those galaxies with measurements of both [S III] $\lambda 6312$ and [S III] $\lambda 9069$, we calculated consistent results of the ionic abundance of S^{2+} , which provide for a reliable use of [S III] $\lambda 6312$. For Cl, we determined the abundance only when both lines are measured to ensure an accurate determination of Cl^{2+} . The ratio of [Cl III] $\lambda 5518$, 5538 is also a density diagnostic (see also Paper IV). Finally, we used T_e (High) to derive the ionic abundances for high and very high ionization species, O^{2+} , Ne^{2+} , Cl^{3+} , and Ar^{3+} , using the [O III] $\lambda 5007$, [Ne III] $\lambda 3869$, [Cl IV] $\lambda 8049$, [Ar IV] $\lambda \lambda 4711, 41$ lines, respectively.

4.1. ICF Tests

The significant line detections from O, Ne, S, Cl, and Ar in the CLASSY sample allow us to calculate their total abundances. For oxygen, the total O/H abundances were calculated in Paper I as the sum of the O^+/H^+ and O^{2+}/H^+ ion fractions, as the emission from O^0 and O^{3+} is negligible in typical star-forming regions (e.g., Berg et al. 2021). The total O/H abundances are reproduced in Table 6 in Appendix C.

On the other hand, unlike oxygen, not all relevant ionic species are observed for the other α -elements, and so it is necessary to use an ICF to account for the unobserved ionic species. To ensure robust total abundance determinations of these elements, we explored the performance of different ICFs.

First, we examine the ICFs of Amayo et al. (2021), which are focused on C, N, Ne, S, Cl, and Ar. These ICFs are based on a grid of photoionization models from the Mexican Million Models database (Morisset 2009), cover the physical properties of both H II regions and integrated low-mass galaxies, covering a broad range of physical properties of extragalactic H II regions and blue compact dwarf galaxies. The parametric expressions of these ICFs depend on the ionization parameter, measured as $O^{2+}/(O^+ + O^{2+})$.

Previous studies focused on the α -elements in SFGs have proposed different sets of ICFs. In this context, we have analyzed the ICFs proposed by Izotov et al. (2006), which are based on photoionization models of N, Ne, O, S, Cl, Ar, and Fe by Stasińska & Izotov (2003). These ICFs also depend on the ionization parameter, but are calibrated for three different ranges of metallicity of integrated SFGs. For Ne, S, and Ar, we have also explored the ICFs of Thuan et al. (1995), which are based on models covering the properties in only local integrated SFGs, while Dors et al. (2013) is based on H II regions and SFGs. The ICFs of both Thuan et al. (1995) and Dors et al. (2013) were calibrated on samples including both H II regions and integrated galaxies. Finally, for Cl, we include a new empirical ICF based on H II regions with high spectral resolution from Domínguez-Guzmán et al. (2022).

The ICFs derived by the different authors depend on the assumptions made for the nebular and stellar properties of the H II regions. For example, different input stellar spectral energy distribution (SED) parameters have been adopted for different studies. Major ingredients are the stellar evolution and atmosphere models. Izotov et al. (2006) and Dors et al. (2013) can be compared directly as their ICFs are based on the same set of stellar models from Starburst99 (Leitherer et al. 1999). Note that Izotov et al. (2006) used the photoionization

models of Stasińska & Izotov (2003) but with the more modern Starburst99 stellar models instead of a previous model generation. Amayo et al. (2021) adopted stellar SEDs obtained with the PopStar code Mollá et al. (2009), whose stellar atmosphere models for massive hot stars are identical to those in Starburst99. However, the isochrones in PopStars are based on Padova evolution models, as opposed to the Geneva models in Starburst99. Figure 4 of Vázquez & Leitherer (2005) highlights the significant differences between SEDs computed with Geneva and Padova tracks. The earlier ICFs of Thuan & Izotov (2005) were obtained with an unevolved zero-age main-sequence population of hot stars using unblanketed atmosphere models of Mihalas (1972). Therefore, these SEDs produce a much harder ionizing spectrum than those discussed before.

Below, we calculate the ionic abundances of Ne, Ar, S, and Cl and use them to analyze the ICFs using the Ne^{2+} , Ar^{2+}/O^{2+} and $(Ar^{2+} + Ar^{3+})/O^{2+}$, $(S^+ + S^{2+})/(O^+ + O^{2+})$, and Cl^{2+}/O^{2+} ionic ratios, respectively. To test the ICFs, we compare to the observed CLASSY galaxy trends. We have used the solar ratio of Ne/O_{\odot} , and S/O_{\odot} for scaling the ICFs with respect to the ionic abundance ratio used in the computation of the total abundance (e.g., Ne^{2+}/O^{2+}). Therefore, those ICFs with similar trends to those used in the CLASSY galaxies analyses should result in total abundances close to the solar abundance. We also examined the resulting total abundance trends of these elements as a second test of the ICFs. In this context, we have analyzed different ICFs to find those most suitable for the CLASSY sample and for SFGs with similar properties to the CLASSY galaxies.

4.2. Ionic Abundances and Relative α -abundances

In principle, Ne, S, Cl, and Ar production depends very little on metallicity because these elements are mainly synthesized in massive stars by the α -capture process. Therefore, any dependence on metallicity of the abundance ratio relative to O might be associated with other properties such as the degree of ionization, dust depletion, the ICF, and/or observational problems (e.g., Amayo et al. 2021). We start by investigating the ICFs below.

4.2.1. Neon

For Ne, only one ionization state is observed, Ne^{2+} (41.0–63.5 eV), such that Ne/O abundances are typically determined using

$$\frac{Ne}{O} = \frac{Ne^{2+}}{O^{2+}} \times ICF(Ne), \quad (2)$$

where Ne^{2+} is determined from the [Ne III] $\lambda 3868$ emission line. Note that a similar equation is used to determine Ne/H such that $Ne/H = Ne^{2+}/H^+ \times ICF(Ne)$. We use the [Ne III] $\lambda 3868$ detection in 38 CLASSY galaxies (see Appendix Table 6) to calculate Ne^{2+} and, subsequently, Ne/O.

We plot the Ne^{2+}/O^{2+} ratio as a function of the ionization parameter ($O^{2+}/(O^+ + O^{2+})$) in the top panel of Figure 2. The different lines illustrate the ICFs analyzed for Ne from Peimbert & Costero (1969, solid black), Izotov et al. (2006, blue dashed, orange dotted-dashed, and navy dotted), Dors et al. (2013, solid green), and Amayo et al. (2021, solid purple). Figure 2 shows that the Ne ICFs of Izotov et al. (2006, low and intermediate metallicity represented as “Z”) and Dors et al. (2013) have similar shapes as the Ne^{2+}/O^{2+} trend for the

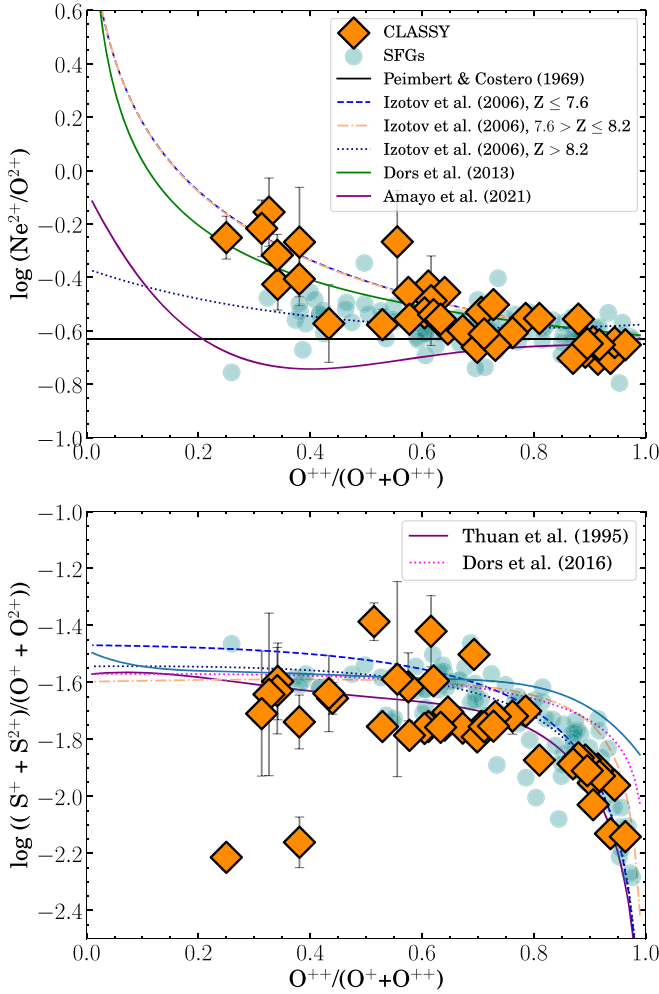


Figure 2. Ionic abundance ratios of Ne, S, and O used to correct for the unseen ionic species. The different lines represent the ICFs derived by Peimbert & Costero (1969), Thuan et al. (1995), Izotov et al. (2006), Dors et al. (2013, 2016), and Amayo et al. (2021). Top: the ratio of $\text{Ne}^{2+}/\text{O}^{2+}$ as a function of the ionization degree measured as $\text{O}^{2+}/(\text{O}^+ + \text{O}^{2+})$ for the CLASSY galaxies with measurements of $[\text{Ne III}] \lambda 3869$. Bottom: the ratio of $(\text{S}^+ + \text{S}^{2+})/(\text{O}^+ + \text{O}^{2+})$ as a function of the ionization degree. The SFGs compiled from the literature are shown in circles. CLASSY galaxies follow the trends given by the ICFs of Dors et al. (2013) for Ne and Izotov et al. (2006) for S. “Z” indicates the value of $12 + \log(\text{O}/\text{H})$.

CLASSY galaxies, while the ICF of Amayo et al. (2021) overestimates the Ne ICF, leading to an overestimate of the total Ne/O ratio with respect to the solar value.

We present the Ne/O versus O/H relation in the top left panel of Figure 3. The comparison samples are also plotted in the Ne/O–O/H plot, showing good agreement with the CLASSY sample for $12 + \log(\text{O}/\text{H}) < 8.4$. Interestingly, the H II region samples have a large dispersion to low Ne/O abundances at $12 + \log(\text{O}/\text{H}) > 8.0$. The Ne/O ratio of the CLASSY galaxies follows the expected constant abundance pattern with an average value of $\log(\text{Ne}/\text{O}) = -0.63 \pm 0.06$, in excellent agreement with the solar abundance reported by Asplund et al. (2021, $\log(\text{Ne}/\text{O})_{\odot} = -0.63 \pm 0.06$). However, for five CLASSY galaxies, we have determined supersolar values of $\log(\text{Ne}/\text{O}) > -0.4$ (J0808+3948, J1144+4012, J1521+0759, J1525+0757, and J1612+081), which is independent of the ICF of Ne involved in this study.

The top right panel of Figure 3 shows the Ne/O ratio as a function of ionization ($\text{O}^{2+}/(\text{O}^+ + \text{O}^{2+})$). It is clear that, for

low-ionization regions (high metallicity), there is a large dispersion extending to high values of Ne/O. If we exclude these outliers, the relation between the ionization degree and Ne/O is constant as is expected. We also used this plot to inspect the applicable range of each ICF used to derive Ne/O. In principle, the applicability of the Ne ICF of Dors et al. (2013) is restricted to values of $\text{O}^{2+}/(\text{O}^+ + \text{O}^{2+}) > 0.2$. This might explain the high values of Ne/O for the 4/5 galaxies with an ionization degree below this limit (excludes J1521+0759 with $\text{O}^{2+}/(\text{O}^+ + \text{O}^{2+}) = 0.56$). However, note that the value of $\text{O}^{2+}/(\text{O}^+ + \text{O}^{2+})$ is highly sensitive to the temperature structure adopted. The five objects with high values of Ne/O are metal-rich, implying a decrease of the T_e -sensitive line $[\text{O III}] \lambda 4363$. Therefore, here, we find Ne/O increases with metallicity, which has been attributed to the depletion of O into dust grains (Izotov et al. 2006; Guseva et al. 2011).

We calculated the dispersion in Ne/O resulting from the use of these ICFs. For the ICFs of Izotov et al. (2006) and Dors et al. (2013), we calculated similar dispersions of 0.06 and 0.07 dex, respectively. The ICF of Amayo et al. (2021) produces a larger dispersion value of 0.12 dex and a strong correlation with metallicity. Therefore, we used and recommend the ICF of Dors et al. (2013) to derive the Ne/O ratios of CLASSY-like galaxies. We report the mean and dispersion values of Ne/O for the CLASSY sample in Table 2.

4.2.2. Sulfur

For sulfur, both S^{2+} (22.3–34.8 eV) and S^+ (10.4–22.3 eV) span the low-ionization zone, although S^+ emission can also extend into the neutral H zone. We do not correct for this issue, but the generally high ionization of the CLASSY sample suggests that the S^+ contribution from outside the H II region should be minimal. On the high-ionization end, we must consider contributions from S^{3+} (34.8–47.2 eV). Thus, we determine the S/O abundance using

$$\frac{\text{S}}{\text{O}} = \left(\frac{\text{S}^+ + \text{S}^{2+}}{\text{O}^+ + \text{O}^{2+}} \right) \times \text{ICF}(\text{S}), \quad (3)$$

where S^+ is determined from the $[\text{S II}] \lambda\lambda 6717, 6731$ emission doublet, and S^{2+} is determined from $[\text{S III}] \lambda\lambda 6312, 9069$. Note that a similar equation is used to determine S/H such that $\text{S}/\text{H} = (\text{S}^+ + \text{S}^{2+})/\text{H}^+ \times \text{ICF}(\text{S})$.

For the CLASSY S/O abundances, we only consider ICFs based on the use of both $[\text{S II}]$ and $[\text{S III}]$. With this criterion, we used the resulting 41 CLASSY galaxies to calculate S^+ , S^{2+} , and, subsequently, S/O. In this analysis, we used the ICFs of Amayo et al. (2021), Dors et al. (2016), and Thuan et al. (1995). Note that some ICFs only use one of the S ions. We plot the $(\text{S}^+ + \text{S}^{2+})/(\text{O}^+ + \text{O}^{2+})$ ratio as a function of the ionization parameter ($\text{O}^{2+}/(\text{O}^+ + \text{O}^{2+})$) in the bottom panel of Figure 2. With the exception of two low-ionization outliers, all three ICFs trace the trend of the CLASSY sample well. Using all ICFs, we calculated three sets of CLASSY S/O abundances. All three S/O sets had dispersions around 0.15 dex, but the ICF of Thuan et al. (1995) provided the closest values of S/O to solar ($\log(\text{S}/\text{O}) = -1.57$). Based on this analysis, we used and recommend the ICF provided by Izotov et al. (2006).

The resulting CLASSY S/O abundances are plotted in Figure 3 as a function of metallicity (left column) and ionization parameter (right column). The comparison samples

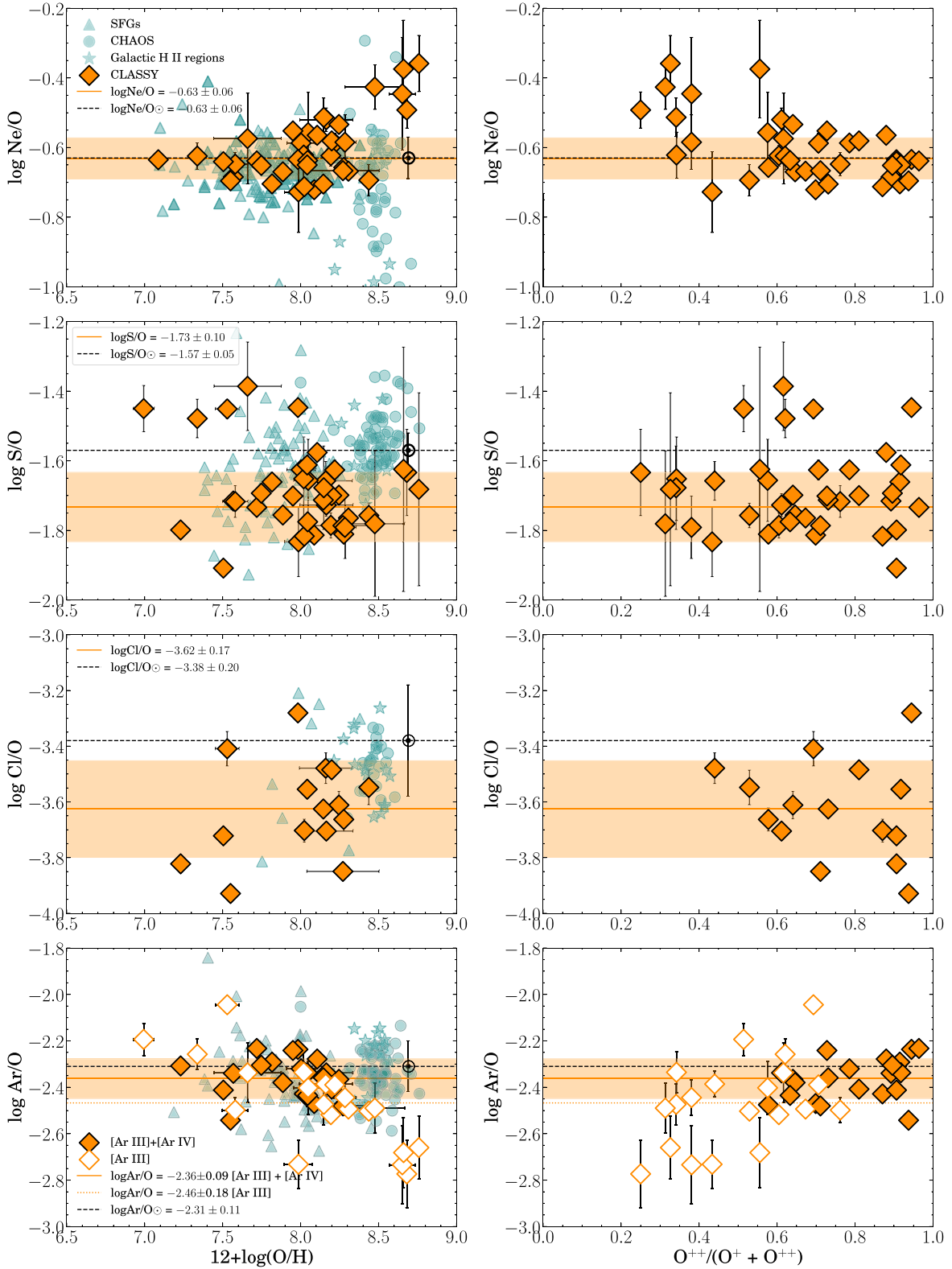


Figure 3. The Ne/O, S/O, Cl/O, and Ar/O ratios vs. metallicity (left) and ionization degree (right) relationships for the CLASSY galaxies. In principle, the ICFs are corrected by ionization effects. The additional SFGs are from Berg et al. (2012, 2016, 2019), Izotov et al. (2006, 2012, 2017), H II regions from the CHAOS survey (Rogers et al. 2021) of M33, and Galactic H II regions from Arellano-Córdova et al. (2020, 2021). For Cl, we have also added three galaxies of Izotov et al. (2021) with measurements of [Cl III] $\lambda\lambda 5518, 5531$ for comparison. The black solid symbol and dashed line represent the solar abundance of Asplund et al. (2021). The mean and dispersion values of the abundance ratios are illustrated with a solid line and shadow box color coded for the CLASSY galaxies. For Ar/O, we present two different results depending on which emission lines are used to determine the total abundance. The filled symbols represent the value of Ar/O derived using [Ar III] + [Ar IV], while empty symbols illustrate the value of Ar/O derived using [Ar III]. For Ar/O, the dashed and solid lines indicate the mean and standard deviation of solid and empty symbols, respectively.

Table 2

Mean and Standard Deviation Values of Ne/O, S/O, Cl/O, and Ar/O for the CLASSY Sample Galaxies

log X/O	N	$\mu \pm \sigma$	Lines	ICF
Ne/O	34	-0.63 ± 0.06	[Ne III]	(1)
S/O	31	-1.73 ± 0.10	[S II] + [S III]	(2)
Cl/O	15	-3.60 ± 0.17	[Cl III]	(2)
Ar/O	20	-2.46 ± 0.18	[Ar III]	(2)
Ar/O	22	-2.36 ± 0.09	[Ar III] + [Ar IV]	(2)

Note. (1) Dors et al. (2013), (2) Izotov et al. (2006). For the S/O ratios, we discard those galaxies with high S/O. The mean and dispersion values considering only the measurement of [Ar III] for 42 galaxies are -2.43 ± 0.16 .

are also plotted in the S/O–O/H plot, showing good agreement with the CLASSY sample for $12+\log(\text{O}/\text{H}) < 8.4$. We also noticed in Figure 3 that the sample of SFGs of Izotov et al. (2006) shows a large dispersion but with most of the sample centered on the solar abundance. Note also the large uncertainties of the metal-rich galaxies. In a similar way, the sample of H II regions shows a good agreement with the solar abundance in comparison with the CLASSY galaxies over the same range of metallicity.

We note that five galaxies have S/O values that are higher than the main CLASSY sample of S/O: J0127–0619, J0405–3648, J0944+3442, J1132+5722, and J1253–0312. To confirm the high values of S/O, we inspect the ionic abundance of S^{2+} derived using [S III] $\lambda 6312$ and [S III] $\lambda 9069$. For galaxies with both measurements, we find a consistent agreement between the value of S^{2+} derived using [S III] $\lambda 6312$ and [S III] $\lambda 9069$ (i.e., J0405–3648 and J1132+5722). Further, we examined whether the adopted T_e affects the derived S/O for the five outliers. Domínguez-Guzmán et al. (2019) and Esteban et al. (2020) show that changes in the temperature structure introduce a slight variation to the S/O ratio (and Cl/O and Ar/O) increasing with metallicity, in particular when the two-zone temperature structure is used.

In our analysis, for J0405–3648 and J1132+5722, we use the direct measurement of $T_e[\text{S III}]$ (or $T_e(\text{Int.})$) to estimate S^{2+} , and for the rest of galaxies (J0127–0619, J0944+3442, and J1253–0312) with high S/O, we use the adopted temperature relations (see Section 3) to estimate $T_e(\text{Int.})$. We estimate the mean value between $T_e(\text{Low})$ and $T_e(\text{High})$ whose result should be a proxy of $T_e(\text{Int.})$ (see also Domínguez-Guzmán et al. 2019). We have used this procedure to preclude that the high value of S/O could be due to the T_e selected for those regions since $T_e[\text{S III}]$ might be affected by telluric lines, a possible blend of [S III] $\lambda 6312$ with [O I] $\lambda 6300$, or reddening corrections that are biased low. We find that, for these individual galaxies, the only two regions that show a significant change in the results are J0944–0038 and J1253–0312. Therefore, part of those differences might be associated with the estimate of $T_e[\text{S III}]$. In this context, we have excluded those five galaxies for our analysis of S. We determine a mean value of $\log(\text{S}/\text{O}) = -1.73 \pm 0.10$, which is 0.16 dex lower than the solar value of $\log(\text{S}/\text{O})_\odot = -1.57 \pm 0.05$ using a number of 35 galaxies since we have discarded the five outliers galaxies.

4.2.3. Chlorine

The CLASSY sample provides the rare opportunity to trace the chemical abundances of Cl. The production of Cl is based

Table 3Ionic Abundances of the CLASSY Galaxies with Detection of Both [Cl III] $\lambda\lambda 5518,38$ and [Cl IV] $\lambda 8049$ in CLASSY

CLASSY	[Cl IV] $\lambda 8049$	^a Cl ²⁺	^b Cl ³⁺	O ₃₂
J0944-0038	0.19 ± 0.01	...	3.76	8.2
J1044+0353	0.22 ± 0.03	3.18	3.73	3.6
J1150+1501	0.09 ± 0.02	4.40	3.65	2.9
J1225+6109	0.12 ± 0.03	4.08	3.65	6.8
J1253-0312	0.21 ± 0.02	4.22	3.90	7.5
J1323-0132	0.25 ± 0.01	...	3.77	38.0
J1448-0110	0.16 ± 0.03	4.13	3.82	7.3
J1545+0858	0.22 ± 0.01	...	3.78	9.2

Notes.

^a In units of $12+\log(\text{Cl}^{2+}/\text{H}^+)$.

^b In units of $12+\log(\text{Cl}^{3+}/\text{H}^+)$. The ionization parameter is defined as $\text{O}_{32} = [\text{O III}] \lambda 5007 / [\text{O II}] \lambda 3727$.

on the radioactive decay of ³⁷Ar formed by a single neutron capture of ³⁶Ar (see Clayton 2003; Esteban et al. 2015). For Cl, typically only one ionization state is observed, Cl²⁺ (23.8–39.6 eV), such that Cl/O abundances are typically determined using

$$\frac{\text{Cl}}{\text{O}} = \frac{\text{Cl}^{2+}}{\text{O}^{2+}} \times \text{ICF}(\text{Cl}), \quad (4)$$

where Cl²⁺ is measured via the [Cl III] $\lambda\lambda 5518,5538$ doublet (see Paper IV). Note that a similar equation is used to determine S/H such that $\text{Cl}/\text{H} = \text{Cl}^+/\text{H}^+ \times \text{ICF}(\text{Cl})$. For our analysis of Cl, we use a sample of 15 CLASSY galaxies with significant detections of [Cl III] to determine the Cl²⁺ abundance and, subsequently, Cl/O.²⁴

While [Cl III] $\lambda 5518,5538$ are the brightest Cl lines in SFGs, and contributions from other ionization states of Cl are typically negligible (e.g., Esteban et al. 2015), we detect Cl³⁺ via [Cl IV] $\lambda 8049$ in eight CLASSY galaxies (see Table 3). With an ionization potential of ~ 39.6 eV, this line is only detected in high-ionization objects (e.g., Esteban et al. 2015). We detect both Cl²⁺ and Cl³⁺ for five CLASSY galaxies, enabling a more direct measure of chlorine using $\text{Cl} = \text{Cl}^{2+} + \text{Cl}^{3+}$. However, Cl⁺ has an ionization potential of 13.0–23.8 eV, similar to O⁺, and so an ICF should still be used to account for the potentially significant contribution from Cl⁺ (Esteban et al. 2015; Arellano-Córdova et al. 2020; Amayo et al. 2021).

We compared Cl ICFs from Izotov et al. (2006), Amayo et al. (2021), and Domínguez-Guzmán et al. (2022). We found that the ICF of Izotov et al. (2006) has the least dependence on metallicity and ionization parameter, and, thus, adopt the Cl ICF from Izotov et al. (2006) to derive Cl/O abundances for CLASSY. We show the resulting Cl/O abundances versus O/H in the third row of Figure 3. On average, we find the CLASSY galaxies to have subsolar Cl/O abundances, with a mean value of $\log(\text{Cl}/\text{O}) = -3.62 \pm 0.17$. This value is 0.24 dex lower than the solar value, but is consistent with previous studies of SFGs (e.g., Izotov et al. 2006, 2017). We

²⁴ Note that [Cl III] $\lambda\lambda 5518,5538$ detections were not possible in the LBT/MODS spectra of three CLASSY galaxies (J0944–0038, J1323–0132, and J1545+0858) due to the wavelength gap between the blue and red arms (see Figure 2 of Arellano-Córdova et al. 2022b).

note that similar trends are obtained using the ICFs of Amayo et al. (2021) and Domínguez-Guzmán et al. (2022).

On the other hand, Arellano-Córdova et al. (2020) used a sample of Galactic H II regions to derive Cl/O abundances using the same ICFs as this work, but found a good agreement with $\log(\text{Cl}/\text{O})_{\odot} = -3.38 \pm 0.20$ (Asplund et al. 2021). Similarly, Rogers et al. (2022) found consistent results with $\text{Cl}/\text{O}_{\odot}$ for the CHAOS sample of H II regions in M33 using the ICF of Amayo et al. (2021). However, the photospheric solar Cl abundance is somewhat uncertain, making it difficult to assess the significance of the subsolar Cl/O abundances of CLASSY. Nonetheless, it is interesting that the integrated S/O and Cl/O abundances of the CLASSY galaxies (and other dwarf SFGs, e.g., Berg et al. 2012, 2016) are lower than the abundances of individual H II regions within galaxies (e.g., Izotov et al. 2006).

The right column of Figure 3 shows the Cl/O ratio with respect to the ionization parameter. We do not find a significant correlation of Cl/O with the ionization parameter, although there is a large dispersion in the data. This dispersion may be due to observational uncertainties associated with the faintness of the [Cl III] lines. Higher signal-to-noise ratio (S/N) [Cl III] and [Cl IV] observations are needed to determine how observational and ICF uncertainties are affecting the Cl/O–O/H trend.

4.2.4. Argon

For Ar, only the Ar^{2+} ionization state is observed for the majority of the CLASSY optical spectra via detections of [Ar III] $\lambda 7135$ (significantly detected in 43 galaxies). Additionally, Ar^{3+} (40.74–59.81 eV) is observed as [Ar IV] $\lambda\lambda 4711, 4740^{25}$ for 22 of these CLASSY galaxies such that $\text{Ar}^{2+} + \text{Ar}^{3+}$ can be used for Ar abundance determinations. However, the ionization potential of Ar^+ (15.76–27.63 eV) overlaps with the low-ionization zone. Therefore, an ICF must be used to account for the unseen Ar^+ , and sometimes Ar^{3+} , ions in Ar abundance determinations using the following:

$$\frac{\text{Ar}}{\text{O}} = \frac{\text{Ar}^{2+} + \text{Ar}^{3+}}{\text{O}^{2+}} \times \text{ICF}(\text{Ar}). \quad (5)$$

Note that a similar equation is used to determine Ar/H such that $\text{Ar}/\text{H} = (\text{Ar}^{2+} + \text{Ar}^{3+})/\text{H}^+ \times \text{ICF}(\text{Ar})$. Additionally, some works only use Ar^{2+} in their ICFs and abundance calculations.

We present Ar abundances using two different approaches: (i) using both [Ar III] $\lambda 7135$ and [Ar IV] $\lambda\lambda 4711, 4741$ lines ($\text{S}/\text{N} \geq 3$) for a sample of 22 SFGs (the preferred method) and (ii) using only [Ar III] $\lambda 7135$ ($\text{S}/\text{N} \geq 3$) for the remaining 20 galaxies with [Ar III] $\lambda 7135$ detections. We test different ICFs for Ar from Thuan et al. (1995), Izotov et al. (2006), and Amayo et al. (2021). For method (i) using only [Ar III], the $\text{ICF}(\text{Ar}^{2+})$ results in a strong dependence on metallicity for $12 + \log(\text{O}/\text{H}) > 8.2$ and a large dispersion up to 0.16 dex. For method (ii) using both [Ar III] and [Ar IV], we find that the $\text{ICF}(\text{Ar}^{2+} + \text{Ar}^{3+})$ of Izotov et al. (2006) and Amayo et al. (2021) are in excellent agreement, providing similar mean and dispersion values of $\log(\text{Ar}/\text{O}) = -2.36 \pm 0.09$ and $\log(\text{Ar}/\text{O}) = -2.35 \pm 0.09$, respectively. The $\text{ICF}(\text{Ar}^{2+} + \text{Ar}^{3+})$ of Thuan et al. (1995) also provides similar results.

²⁵ Note that [Ar IV] $\lambda 4711$ is often blended with the He I $\lambda 4713$ line in low- to moderate-resolution spectra ($R \lesssim 2000$), and so care must be taken to account for the He I contribution to the flux.

In the bottom row of Figure 3, we present the Ar/O abundances for the CLASSY sample. The open diamonds represent those SFGs with only detections of [Ar III] while the solid diamonds represent those with detections of both [Ar III] and [Ar IV]. For the latter subset, we also determined Ar/O using only the detection of [Ar III] and found differences between the two methods of up to $\Delta \log(\text{Ar}/\text{O}) \lesssim 0.10$ dex, but with $\Delta \log(\text{Ar}/\text{O}) \lesssim 0.05$ dex for most galaxies. This implies that robust Ar/O determinations require detections of both [Ar III] and [Ar IV], particularly for high ionization objects (see also, Berg et al. 2021). Therefore, we adopt the $\text{ICF}(\text{Ar}^{2+} + \text{Ar}^{3+})$ of Izotov et al. (2006; see also Table 2).

Using the more robust [Ar III] + [Ar IV] sample of CLASSY Ar/O abundances, we find a mean value of $\log(\text{Ar}/\text{O}) = -2.36 \pm 0.09$ that is in good agreement with both the solar abundance ($\log(\text{Ar}/\text{O})_{\odot} = -2.31 \pm 0.11$) and the literature samples at lower metallicities ($12 + \log(\text{O}/\text{H}) < 8.3$). If we include the [Ar III]-only sample, however, then the Ar/O versus O/H relation shows an unexpected trend with metallicity at higher metallicities. Other studies of integrated galaxy spectra also have reported a dependence with metallicity in the Ar/O–O/H relation (e.g., Pérez-Montero et al. 2007; Kojima et al. 2021). On the other hand, the literature sample of H II regions is consistent with the solar Ar/O ratio even at higher metallicities.

The method (i) Ar/O abundances also show a trend with $\text{O}^{2+}/(\text{O}^+ + \text{O}^{2+})$ in the right column of Figure 3 (open diamonds), which could be associated with the performance of the ICF with respect to the ionization degree. In comparison, the values of Ar/O for galaxies with measurements of [Ar IV] are constant for $\text{O}^{2+}/(\text{O}^+ + \text{O}^{2+}) > 0.6$. Therefore, the performance of different ICFs may be more uncertain at high metallicities and a low-ionization parameter (e.g., Amayo et al. 2021).

4.2.5. $\text{Ar}^{2+}/\text{S}^{2+} \sim \text{Ar}/\text{S}$

We investigated the behavior of the abundance ratio of $\text{Ar}^{2+}/\text{S}^{2+}$. With similar ionization potentials of 27.6 and 23.3 eV for Ar^{2+} and S^{2+} , respectively, these two ions both trace the intermediate ionization state of the gas (e.g., Berg et al. 2021). In Figure 4, we present $\log(\text{Ar}^{2+}/\text{S}^{2+})$ with respect to the metallicity (left panel) and ionization degree (right panel) for both the CLASSY sample and the comparison sample. For the CLASSY sample, we calculate a mean of $\log(\text{Ar}^{2+}/\text{S}^{2+}) = -0.58 \pm 0.06$, which is in excellent agreement with the values reported in Kennicutt et al. (2003b) and Croxall et al. (2016) for individual H II regions in M101. However, Croxall et al. (2016) showed that $\text{Ar}^{2+}/\text{S}^{2+}$ decreases significantly in low-ionization objects ($\text{O}^+ / (\text{O}^+ + \text{O}^{2+}) \geq 0.6$; see also Figure 4) due to the contribution of Ar^+ (dotted line in Figure 4). The CLASSY galaxies stay constant at larger values of O^+/O for most of the sample. This implies that the $\text{Ar}^{2+}/\text{S}^{2+}$ abundance ratio serves as a good approximation for the total Ar/S ratio, $\text{Ar}^{2+}/\text{S}^{2+} \sim \text{Ar}/\text{S}$ (i.e., removing the use of the ICFs due to the similar ionization potentials).

While the $\text{Ar}^{2+}/\text{S}^{2+} \sim \text{Ar}/\text{S}$ trend is relatively constant and the Ar/O trends from [Ar III]+[Ar IV] are similarly well behaved in Figure 3, the S/O trends are more messy due to large ICF uncertainties (see discussion in Section 4.2.2). Therefore, our analysis of Ar/S suggests that the most probable explanation for the low values of S/O, and subsequent large dispersion, is due to the ICF of S used. This implies that the adopted Izotov et al. (2006) ICF might be useful for individual

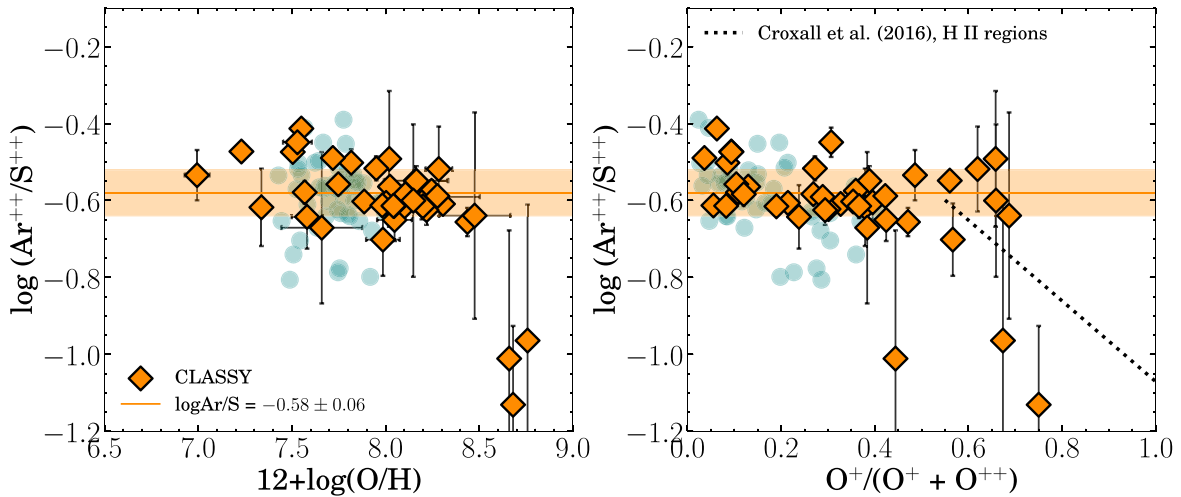


Figure 4. The ionic abundance ratio of $\text{Ar}^{2+}/\text{S}^{2+}$ as a function of metallicity (left) and O^{+}/O (right) for CLASSY. The circles are SFGs of the sample described in Section 2. The mean and standard deviation value of $\log(\text{Ar}^{2+}/\text{S}^{2+})$ is illustrated with a solid line color coded with CLASSY. The result of $\log(\text{Ar}^{2+}/\text{S}^{2+}) = -0.58 \pm 0.06$ is in agreement with those found in H II regions (Kennicutt et al. 2003b; Croxall et al. 2016) at $\text{O}^{+}/\text{O} < 0.60$. While the value of $\log(\text{Ar}^{2+}/\text{S}^{2+})$ for CLASSY stays constant, low-ionization H II regions show a significant decrement at high values of $\text{O}^{+}/(\text{O}^{+} + \text{O}^{2+}) \geq 0.60$ (Croxall et al. 2016). This decrement is related to the increased contribution of Ar^{+} in low-ionization objects. The green solid line quantifies the decrement derived by Croxall et al. (2016) for H II regions in M101.

H II region abundances, but may not be appropriate for integrated galaxy spectra.

4.3. Total versus Relative Abundances

In this section, we present the total abundances of Ne, S, Cl, and Ar and compare to their respective relative α -abundances. In Figure 5, we show the comparison of the Ne/O abundance ratio derived for the CLASSY galaxies. In addition, we have added the results of Miranda-Pérez & Hidalgo-Gómez (2023), who derived multiple chemical abundances in a sample of SFGs from the SDSS. For Ne/O, Miranda-Pérez & Hidalgo-Gómez (2023) used the ICF of Torres-Peimbert et al. (1989; $\text{Ne}^{2+}/\text{O}^{2+} \approx \text{Ne}/\text{O}$), which is based on the similarity of the ionization potentials of Ne^{2+} and O^{2+} .

The results of Miranda-Pérez & Hidalgo-Gómez (2023) also show that the Ne/O ratio increases with metallicity at $12+\log(\text{O}/\text{H}) \sim 8.21$ (see also Izotov et al. 2011). In fact, for CLASSY and the sample from the literature (SFGs and H II regions), we obtained similar results showing a constant trend with metallicity (see Figure 3). Although it is unclear what is the role of the ICF(Ne) at a low-ionization degree, the ICFs in SFGs of Ne should be assessed, in particular, in metal-rich galaxies ($12+\log(\text{O}/\text{H}) > 8.2$). However, chemical evolution models predict a secondary production of Ne at high metallicities in a similar way to N. In such a scenario, Ne increases more quickly than O above the solar value (see Figure 39 of Kobayashi et al. 2020a).

We also compare S/O with respect to the sample of Miranda-Pérez & Hidalgo-Gómez (2023). Again, in Figure 5, we show the S/O versus S/H for the CLASSY galaxies. In fact, for the set of galaxies of Miranda-Pérez & Hidalgo-Gómez (2023), the results show lower values of S/O in comparison with CLASSY ($12+\log(\text{S}/\text{H}) = 5.5\text{--}6.5$), while a few objects show high values of S/O. Miranda-Pérez & Hidalgo-Gómez (2023) also report a strong trend of S/O with metallicity, but it is unclear how many galaxies with measurements of [S II] and [S III] are used to derive S/O and S/H, since the use of only S^{+} ([S II] $\lambda\lambda 6717, 31$) can introduce a strong dependence of S/O with metallicity (see Amayo et al. 2021). However, we

note that the sample of SDSS galaxies shows lower abundances relative to the solar value, in agreement with the S/O trends of the CLASSY galaxies (see also Figure 3).

In the bottom panel of Figure 5, we also compare the Cl/O ratios of the CLASSY galaxies with the results of Miranda-Pérez & Hidalgo-Gómez (2023). While with CLASSY we get a constant trend with Cl/H, the sample of Miranda-Pérez & Hidalgo-Gómez (2023) shows a slight trend of Cl/O as Cl/H increases. However, the dispersion in the Cl/O versus O/H relationship (see also Figure 3) plus the few measurements in the sample Miranda-Pérez & Hidalgo-Gómez (2023) provide a less robust comparison.

As an additional comparison, in Figure 5, we show the Ar/O ratios with respect to Ar/H for CLASSY and the results of Miranda-Pérez & Hidalgo-Gómez (2023). We find a good agreement with the sample of Miranda-Pérez & Hidalgo-Gómez (2023) around the range of $12+\log(\text{Ar}/\text{H}) = 5.3\text{--}5.9$. However, at high values of Ar/H, we found an opposite behavior than Miranda-Pérez & Hidalgo-Gómez (2023), whose sample shows a significant trend with the Ar/H abundance. An opposite behavior is also found at lower values of $12+\log(\text{Ar}/\text{H}) \sim 5$. Recently, Arnaboldi et al. (2022) analyzed the abundance pattern of the O/Ar versus Ar/H relation for a sample of planetary nebulae in M31. Arnaboldi et al. (2022) found that the highest values of O/Ar (~ 2.5) are the lowest values of Ar/H ~ 6 . With CLASSY, there are only a few galaxies with $\text{Ar}/\text{H} \geq 6$, and such a correlation is unclear. However, the sample of galaxies of Miranda-Pérez & Hidalgo-Gómez (2023) shows that Ar/O increases as the total abundance of Ar increases. A significant correlation between Ar/O and Ar/S is not expected due to the origin of these elements. However, chemical evolution models predict that such a correlation might be due to the additional contribution of Ar from Type-Ia SNe (Kobayashi et al. 2020a, 2020b; Arnaboldi et al. 2022). Such a scenario suggests that the production of Ar can be due to both CCSNe and Type-Ia SNe, although a large time delay is expected until Ar can be enriched by the latter mechanism.

At lower values of Ar/H (and low metallicity), the trend with Ar/O is constant as expected for the nucleosynthesis origin of Ar and O, which are produced by CCSNe (see Figures 3 and 5). For the lowest values of Ar/H ~ 5 , the two different trends shown in CLASSY and the sample of

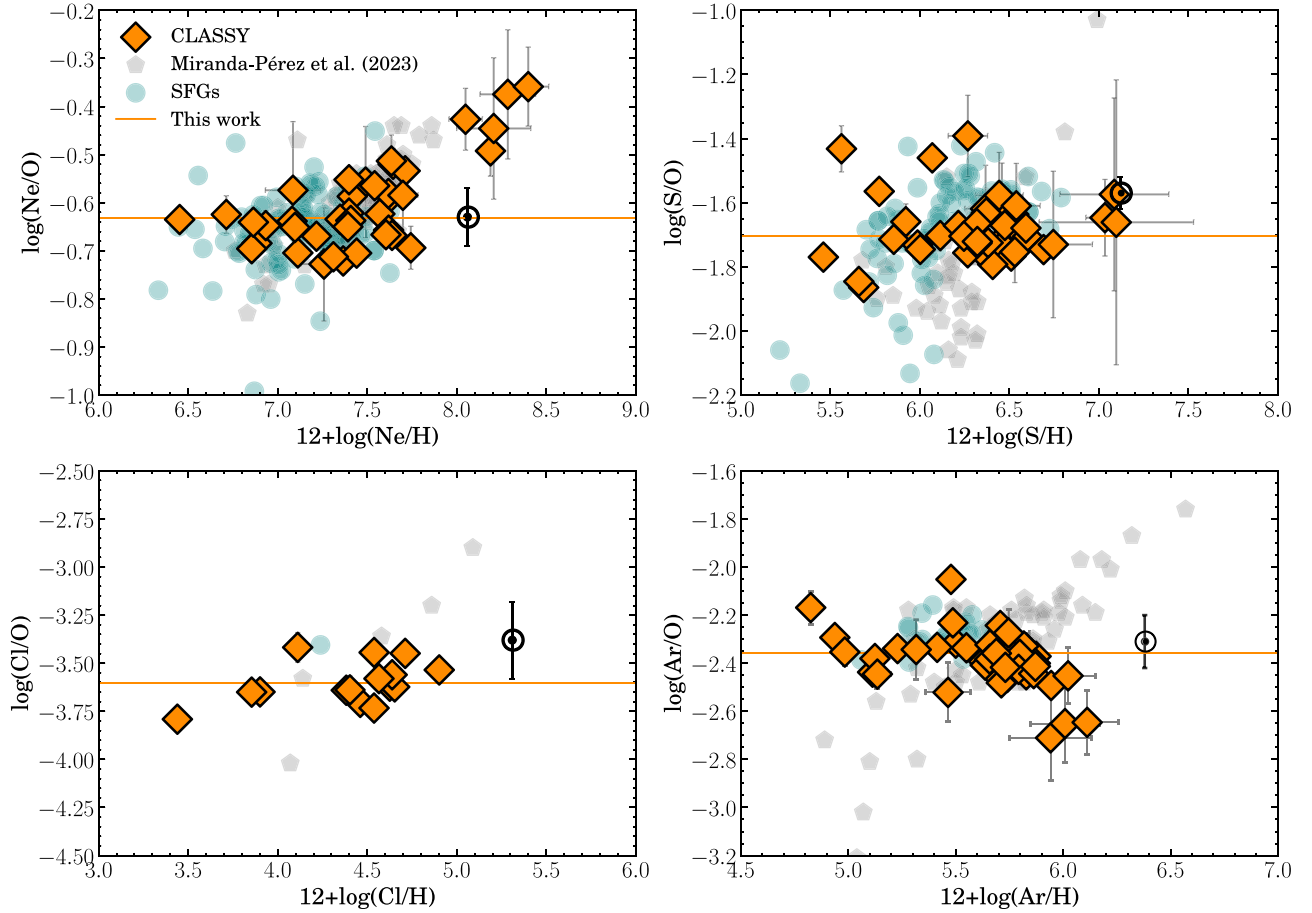


Figure 5. The relative abundances of Ne, S, Cl, and Ar with respect to Ne/O, S/O, Cl/O, and Ar/O. The circles and pentagons represent the sample of SFGs compiled in this study and 85 $z \sim 0$ SFGs of Miranda-Pérez & Hidalgo-Gómez (2023). The solar symbol in each plot indicates the photosphere abundance of Ne, S, Cl, and Ar of Asplund et al. (2021). The solid line indicates the fit of the abundance ratios for CLASSY (see Figure 3). The abundances of the sample of SFGs of Miranda-Pérez & Hidalgo-Gómez (2023) were determined using different ICFs than those implied in this study. The Ne/O and Ar/O ratios show a significant trend with respect to the relative abundances of Ne and Ar.

Miranda-Pérez & Hidalgo-Gómez (2023) might be related to the ICF and its performance in the integrated spectra of galaxies with a lower degree of ionization.

In general, the abundance patterns of Ne, S, and Ar of the CLASSY galaxies follow the expected trends for nucleosynthesis (with important bias at high metallicities). Another possible cause of the behavior is that the abundances of Ne, S, and Ar might be affected by the interplay between stellar yields and the stellar life of massive stars (Matteucci & Chiappini 2005). Using chemical evolution models, Matteucci & Chiappini (2005) showed that the abundance ratio of [O/S] and [O/Si] (relative to the solar abundance) varies as a function of metallicity due to the nonnegligible contribution of Type Ia SNe (Matteucci & Chiappini 2005; Kobayashi et al. 2020a; Arnaboldi et al. 2022). Therefore, while oxygen is uniquely produced by massive stars, α -elements such as S and Ar might be created in a non-negligible way for different ranges of masses (Matteucci & Chiappini 2005). Chemical evolution models in the solar neighborhood also predict the expected constant behavior for S (and similar for Ne and Si) but with a slight decrease of this abundance as metallicity increases (i.e., [Fe/H] in stars; Kobayashi et al. 2020a).

5. Abundance Patterns in the Early Universe

With JWST providing deep spectra of high-redshift galaxies, the first Ne, S, and Ar abundances have been provided for the

early Universe (e.g., Arellano-Córdova et al. 2022a; Isobe et al. 2023b; Marques-Chaves et al. 2024; Rogers et al. 2024). Using these studies, we can investigate the evolution of relative α -abundance patterns of O, Ne, S, and Ar for the first time. In particular, Isobe et al. (2023b) derived Ne/O, S/O, and Ar/O abundances for a sample of 70 $4 < z < 10$ SFGs compiled from the ERO (Pontoppidan et al. 2022), GLASS (Treu et al. 2022), and CEERS (Finkelstein et al. 2023) programs. Isobe et al. (2023b) used direct T_e measurements for 13 galaxies, but had to assume a $T_e = 15,000 \pm 5000$ K, and $n_e = 300 \text{ cm}^{-3}$ for the remaining 57 galaxies. We, therefore, augment the Isobe et al. (2023b) sample with direct T_e measurements for a $z \sim 11$ galaxy from Marques-Chaves et al. (2024), three $z > 7$ galaxies from Arellano-Córdova et al. (2022a; replacing three galaxies reported in Isobe et al. 2023b), and a $z > 3$ galaxy from the CECILIA survey (Strom et al. 2023; Rogers et al. 2024). In order to consistently compare the CLASSY abundance patterns with $z > 3$ galaxies, we require direct measurements of T_e , derived using either [O III] $\lambda 4363$ or [O III] $\lambda 1666$, and n_e , derived from [O II] $\lambda 3729/\lambda 3726$, with $S/N \geq 4$.

5.1. Cosmic Evolution of Ne/O

In Figure 6(a), we compare the Ne/O abundance pattern of CLASSY with the 10 $z > 3$ SFGs that meet of direct- T_e requirement and have Ne/O measurements. We found that at $z > 3$ the average $\log(\text{Ne/O}) = -0.72 \pm 0.17$. In comparison to

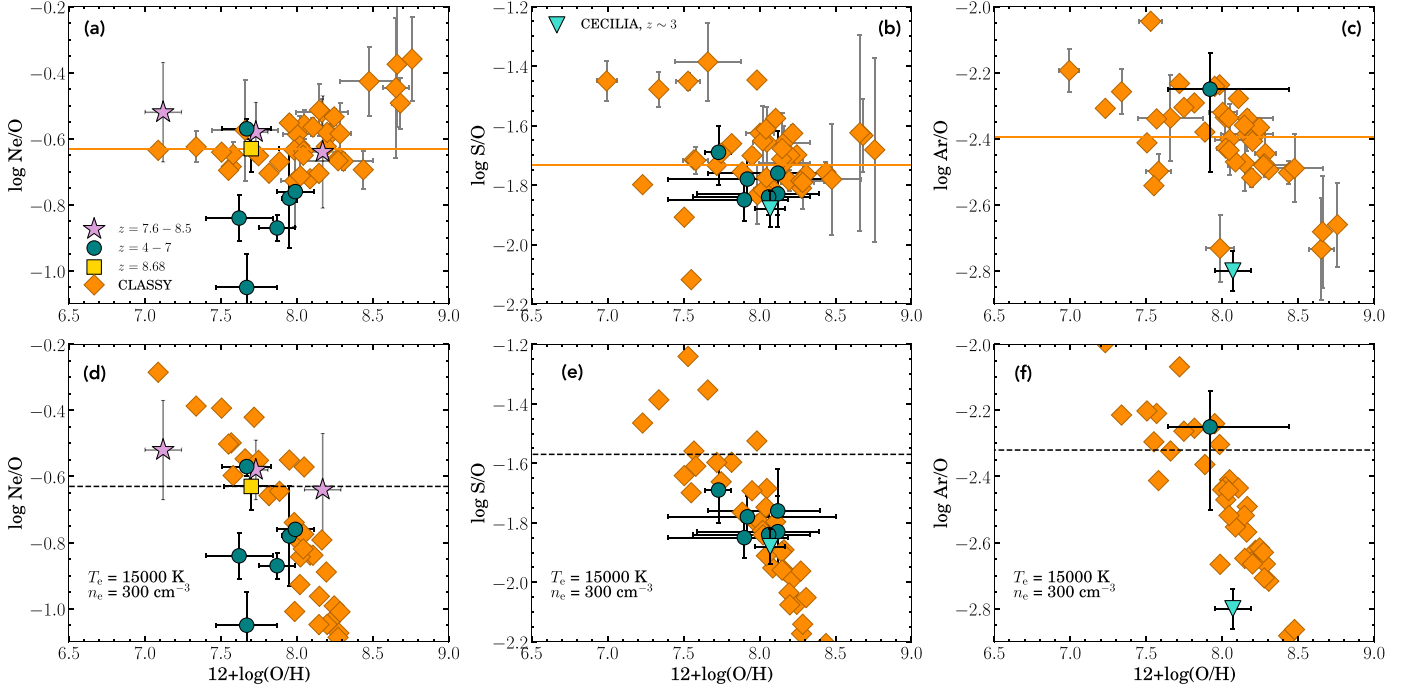


Figure 6. Top: relative α -abundances vs. oxygen abundance for the CLASSY sample ($z \sim 0$; orange diamonds) in comparison with SFGs at $z > 3$ from Rogers et al. (2024; turquoise triangle), Arellano-Córdova et al. (2022b; pink stars), Isobe et al. (2023b; green circles), and Marques-Chaves et al. (2024; gold squares). The error-weighted mean α -ratios are indicated by the solid orange lines in each panel (see also Section 3). Panel (a) shows the Ne/O trend, panel (b) shows the S/O trend, and panel (c) shows the Ar/O trend, with an additional $z \sim 0$ comparison sample from Kojima et al. (2021; blue pentagons). Note that the abundance patterns of S/O and Ar/O of Isobe et al. (2023b) were estimated using $T_e = 15,000 \pm 5000$ K, and $n_e = 300 \text{ cm}^{-3}$. Bottom: the same abundance patterns as shown in the top row, but with CLASSY abundances recalculated assuming $T_e = 15,000 \pm 5000$ K, and $n_e = 300 \text{ cm}^{-3}$ to match the method of the high- z sample in Isobe et al. (2023b). While the low- and high- z trends overlap, the bottom row plots show significant decreasing trends with increasing metallicity and larger dispersions than the trends in the top row. This result shows the importance of characterizing the temperature structure of the gas in SFGs.

the average $\log(\text{Ne}/\text{O}) = -0.63 \pm 0.06$ for the CLASSY sample, the higher-redshift galaxies show similarly large scatter but subsolar Ne/O abundances. On the other hand, the $z = 8.678$ SFG (yellow square) shows an excellent agreement with the solar abundance and the mean values of Ne/O for CLASSY. This result is consistent with the lack of evidence of cosmic evolution of Ne/O as reported in Arellano-Córdova et al. (2022a) for $z > 7$ galaxies using JWST/NIRSpec ERO observations (Pontoppidan et al. 2022; Trump et al. 2023). The low $\log(\text{Ne}/\text{O}) < -1.0$ values in the Isobe et al. (2023b) sample are explained in that work using chemical evolution models of Watanabe et al. (2024). These authors concluded that the models with $M \geq 30 M_\odot$ can reproduce the low values of Ne/O since Ne is reduced due to the high temperature in the carbon-burning layer of these stars, which should be typical at high- z (see, Isobe et al. 2023b).

Low values of Ne/O are also observed in local SFGs, but typically only from H II region spectra at high metallicities ($12 + \log(\text{O}/\text{H}) > 8.0$; see Figure 3). The cause of these low values of Ne/O is still unclear, but it might be related to the ionization structure of the gas, or to ICFs that have been poorly calibrated for the extreme conditions and integrated spectra of high- z galaxies. Therefore, to evaluate this discrepancy in the abundance patterns of Ne/O, it is crucial to increase the number of galaxies at $z > 3$ with accurate T_e -based abundances. In this context, the present study with CLASSY provides a robust foundation to compare the Ne/O abundances of high- z galaxies and evaluate its chemical evolution across cosmic time.

5.2. Cosmic Evolution of S/O

Figure 6(b) shows the evolution of the S/O abundance pattern. Unfortunately, only two high- z galaxies have T_e -based S/O measurements (one from Isobe et al. 2023b; and one from Rogers et al. 2024). Thus, we also consider galaxies from Isobe et al. (2023b) with S/O measurements but no T_e detection in order to increase our sample of high- z galaxies to seven. Note that we have added only those galaxies whose uncertainties are also reported (i.e., avoiding upper limit results). In this context, it is crucial to be careful with the interpretation of relative abundances in our comparison of CLASSY with high- z galaxies due to the missing detection of T_e . However, these results can provide a general view of the high- z abundance distributions.

Interestingly, the high- z sample in Figure 6(b) shows very little scatter and is in good agreement with the average $z \sim 0$ CLASSY trend. In particular, the mean S/O abundance of the high- z sample ($\log(\text{S}/\text{O}) = -1.88 \pm 0.06$) is consistent with the average value of the CLASSY sample ($\log(\text{S}/\text{O}) = -1.73 \pm 0.10$), suggesting there is no cosmic evolution of the S/O abundance. However, it is important to mention that the high- z S/O values are computed using only the measurements of $[\text{S II}] \lambda\lambda 6717, 31$ (see Figure B1 of Isobe et al. 2023b). The use of solely the low-ionization S lines might introduce significant correlations in the S/O trend with the ionization parameter and metallicity (e.g., Amayo et al. 2021).

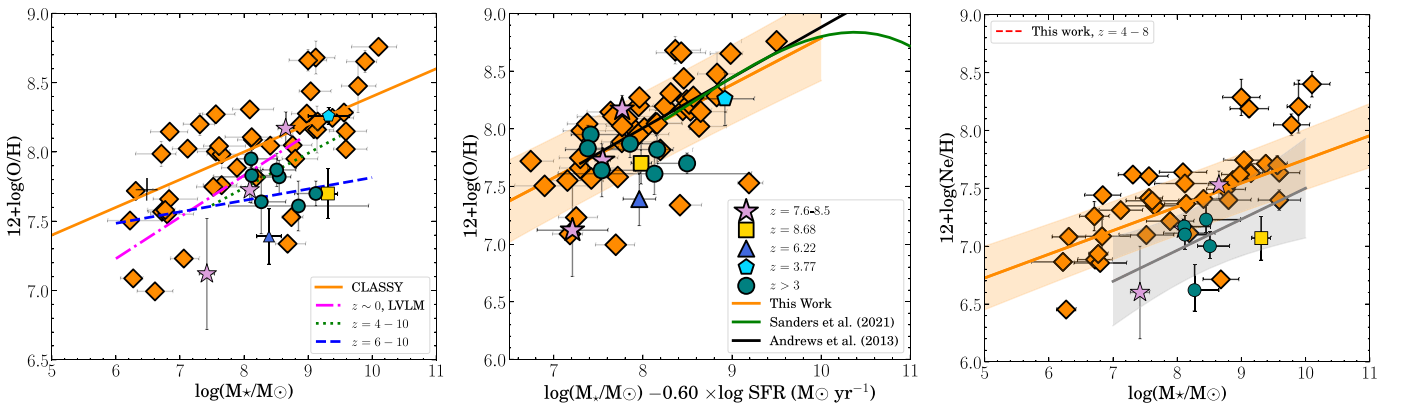


Figure 7. Left: the evolution of the MZR. The $z \sim 0$ CLASSY sample is shown as orange diamonds, with the best-fit MZR from Berg et al. (2022) shown as an orange line. In comparison, we also plot high- z galaxies from Arellano-Córdova et al. (2022a; $z > 7$; pink stars), Nakajima et al. (2023; $z > 4$; teal circles), and Marques-Chaves et al. (2024; $z \sim 9$; yellow square); and MZRs from Berg et al. (2012; $z = 0$), Nakajima et al. (2023; $z = 4-10$), and Curti et al. (2024; $z = 6-10$). Center: the evolution of the FMR for CLASSY in comparison to $z > 3$ galaxies with T_e -direct abundance determinations. The green line is the projection fit of the FMR of Sanders et al. (2021; at $z = 0-3$) and Andrews & Martini (2013; at $z \sim 0$) using stacked spectra with metallicity determined using strong-line methods and the T_e -sensitive method, respectively. CLASSY and $z > 3$ galaxies follow the FMR with no apparent evolution. Right: evolution of the MNeR. The black solid line represents the best fit to the CLASSY data, while the gray line illustrates the fit to the high- z galaxy sample. There appears to be an evolution of the MNeR: higher-redshift galaxies have both a steeper MNeR slope of 0.27 ± 0.19 and a lower y -intercept.

5.3. Cosmic Evolution of Ar/O

Here, we consider the cosmic evolution of the Ar/O–O/H trend. Similar to S/O, only the $z \sim 3$ galaxy from Rogers et al. (2024) has a T_e -based Ar/O abundance. We again consider galaxies from Isobe et al. (2023b) with Ar/O measurements but no T_e detection; however, this only adds one galaxy to the high- z sample. With no significant sample of high- z Ar/O abundances, we limit our analysis of Ar/O to the abundance from Rogers et al. (2024) but still show a visual examination in Figure 6(c).

Interestingly, the Ar/O ratio reported in Rogers et al. (2024) at $z \sim 3$ is significantly lower than the average $z \sim 0$ value of the CLASSY sample. However, Figure 3 also shows that four CLASSY galaxies (J0808+3948, J0940+2935, J1144+4015, J1525+0757) have similar values of Ar/O as in Rogers et al. (2024) for a similar $12+\log(\text{O}/\text{H}) > 8.0$. A detailed inspection with a large sample of high- z galaxies (at moderate metallicities) is needed to evaluate the Ar/O evolution. The Ar/O ICFs may also require updated calibrations for integrated galaxy spectra.

5.4. Temperature Effects in Abundance Determinations at High Redshift

The increase of $z > 3$ galaxies with the emission lines necessary to derive α -element abundances is an extraordinary opportunity to investigate the relative chemical enrichment of Ne, S, and Ar. However, some high- z systems lack the auroral line detections necessary for a robust T_e measurement. Accurate chemical abundance determinations require T_e measurements since collisionally excited lines (e.g., [Ne III], [Ar III], and [S III]) depend exponentially on T_e (e.g., Osterbrock & Ferland 2006; Peimbert et al. 2017).

Most high- z abundance measurements still lack T_e measurements and must, therefore, assume fixed T_e and n_e values. In this context, it is important to assess the bias introduced to the relative and total abundance determinations by unknown temperatures. To evaluate this bias, we recalculated the abundance patterns of the CLASSY galaxies following the procedure of Isobe et al. (2023b) when T_e is not available. This procedure uses fixed values of $T_e = 15,000$ K, and $n_e = 300 \text{ cm}^{-3}$.

In the bottom row of Figure 6, we show the Ne/O, S/O, and Ar/O trends as a function of O/H for the CLASSY sample assuming fixed T_e and n_e values. Compared to the T_e -abundances in the top row, the fixed- T_e values show much stronger correlations with metallicity. These trends also extend to lower Ne/O, S/O, and Ar/O values, suggesting that fixed temperatures may underestimate relative α -abundances. Therefore, the implications of comparing samples with abundances derived using different T_e methods/assumptions can lead to significant bias in our interpretation of the chemical enrichment history. Therefore, we stress that, in order to accurately evaluate the chemical evolution of galaxies, a sample of galaxies with high-S/N detections and robust measurements of the T_e -sensitive [O III], [S III], and/or [N II] lines are necessary to reduce possible bias.

6. Scaling Relations of Metals

Here, we discuss the abundance patterns of O, Ne, S, Cl, and Ar as a function of the galaxy properties such as stellar mass and SFR for CLASSY in comparison with the results of $z > 3$ galaxies.

6.1. Mass–Metallicity Relation

MZR is shaped by evolutionary processes associated with the baryon cycle and so provides essential information on the growth and evolution of galaxies (e.g., Lequeux et al. 1979; Tremonti et al. 2004; Maiolino & Mannucci 2019; Nakajima et al. 2023; Curti et al. 2024). Here, we compare the MZR of CLASSY with our high- z ($z > 3$) galaxy sample. The SFR and stellar masses were compiled from the original papers. In Figure 7, we show the MZR for CLASSY derived in Paper I.

First, we compare these results with other local SFGs. In the top panel of Figure 7, we plot the slope (magenta dashed line) derived using the low-mass Local Volume Legacy (LMLVL; $z \sim 0$) of Berg et al. (2012) with T_e direct abundances. The CLASSY sample follows the trend derived for LMLVL SFGs, with a similar slope and with a slight offset to higher metallicities (see also Paper I). In Figure 7, we have also added as pink stars the results of $z > 7$ galaxies analyzed in Arellano-Córdova et al. (2022a). As shown in

Arellano-Córdova et al. (2022a), there is no evidence for evolution of the MZR given that the $z > 7$ galaxies follow the local MZR with the dispersion ($\sigma = 0.29$).

Recently, some authors have focused on understanding the physical processes driving the MZR, and its evolution across cosmic time using a statistical sample of $z > 3$ galaxies (e.g., Nakajima et al. 2023; Curti et al. 2024). Here, we compare the slopes derived in Nakajima et al. (2023) and Curti et al. (2024), who used samples of SFGs obtained from CEERS (Finkelstein et al. 2023), GLASS (Treu et al. 2022), and JADES (Eisenstein et al. 2024), respectively. The range of valid masses for these slopes is $M_* < 10^{9.5} M_\odot$. It is important to note that the slopes derived in such studies depend on the empirical calibrators (with few objects with T_e -metallicities, e.g., Nakajima et al. 2023). Both samples cover similar ranges in redshift ($z = 3-10$). The $z = 4-10$ MZR derived by Nakajima et al. (2023, dashed green line) follows the trend of CLASSY galaxies and the LMLVL sample with a slight offset to lower metallicities. On the other hand, the MZR of galaxies at $z > 6$ is flatter than that of the $z \sim 0$ CLASSY and LVLML samples. Similarly, Curti et al. (2024) found a relatively flat MZR slope for their full $z = 3-10$ sample (0.17 ± 0.03), and a significantly flatter slope (0.11 ± 0.05) for the highest-redshift galaxies in their sample ($z = 6-10$). Such flat slopes have been attributed to a different feedback mechanism dominating in dwarf $M_* < 10^{9.5} M_\odot$ $z \sim 2-3$ galaxies (Li et al. 2023).

Since a steep slope is seen for all masses in the the local CLASSY T_e -method MZR, the shallower slopes of the $z > 3$ MZRs may be the result of using empirical calibrations. On the other hand, the $z > 3$ MZR slopes are compatible with the results derived for $z \sim 0$ green pea and blueberry galaxies using the direct method (Yang et al. 2017), which systematically differs from our CLASSY results. Therefore, a significant sample of $z \sim 3$ galaxies with direct metallicities is fundamental to constrain the MZR to the mild/strong evolution of the MZR at those redshifts (e.g., Sanders et al. 2021; Strom et al. 2023; Rogers et al. 2024). Such a sample could then improve the performance of empirical calibrations, which will play a crucial role in understanding the evolution and shape of the MZR across cosmic time (e.g., Kewley & Ellison 2008; Patrício et al. 2016).

6.2. Fundamental Metallicity Relation

The relation between stellar mass, metallicity, and SFR is the so-called fundamental metallicity relation (FMR; Mannucci et al. 2010), due to the secondary dependence of the MZR (Ellison et al. 2008). The FMR was first characterized for $z = 0-4$, and it is associated with important evolutionary processes in galaxy formation, primarily the infall of pristine gas, which acts to elevate the SFR at the same time as diluting the gas-phase metallicity (e.g., Lara-López et al. 2010; Mannucci et al. 2010; Andrews & Martini 2013; Kumari et al. 2021; Sanders et al. 2021).

The functional form of the FMR was defined by Mannucci et al. (2010) as

$$\mu_\alpha = \log(M_*) - \alpha \cdot \log(\text{SFR}), \quad (6)$$

where stellar mass and SFR have units of M_\odot and $M_\odot \text{yr}^{-1}$, respectively. Adopting this equation, we determine the best-fit FMR to the CLASSY data to have $\alpha = 60$ such that

$$12 + \log(\text{O}/\text{H}) = (0.40 \pm 0.08) \times \mu_{60} + (4.7 \pm 0.65), \quad (7)$$

with a standard deviation of $\sigma = 0.32$ dex. We illustrate our derived FMR in the middle panel of Figure 7 in comparison to $z > 3$ galaxies with metallicities determined using the direct method. The results of Arellano-Córdova et al. (2020), Jones et al. (2023), Marques-Chaves et al. (2024), and Nakajima et al. (2023) illustrate observations of JWST for $z > 3$ galaxies, while the result of Citro et al. (2024) corresponds to ground-based observations of a lensed galaxy at $z \sim 4$.

We also compare to the FMR of Sanders et al. (2021) and Andrews & Martini (2013). Note, however, both Sanders et al. (2021) and Andrews & Martini (2013) derived their FMRs using stacked spectra of $z \sim 0$ galaxies, but find $\mu_\alpha = 0.60$ and 0.66, respectively, in good agreement with the FMR for CLASSY galaxies. Interestingly, the CLASSY galaxies with the lowest metallicities ($12 + \log(\text{O}/\text{H}) \sim 7.5$) depart from the general trend of the sample and the FMR, (J0405-3646, J1132-5722, J0127-0519, J0337-0502, and J934+5514), although three of these galaxies (J0337-0502, J0405-3646, and J934+5514) have properties that match well with the properties of $z > 7$ galaxies in Arellano-Córdova et al. (2022a) within the uncertainties.

In general, the $z > 3$ sample shows good consistency with the $z = 0$ CLASSY FMR, suggesting no evolution in the FMR for $z = 0-3$. Recently, Nakajima et al. (2023) analyzed the cosmic evolution of the FMR for $z = 4-10$ galaxies. These authors reported that galaxies at $z < 8$ are consistent with the local FMR but find evidence for an evolution at $z > 8$, suggesting a fundamental change in the physical processes acting on galaxies at the earliest epochs. Similarly, Curti et al. (2024) report an evolution away from the local FMR for galaxies at $z > 6$.

Although we do not see strong evidence for an FMR evolution in the middle plot of Figure 7, the sample size is small. As before, however, it is important to note that the results of Nakajima et al. (2023) and Curti et al. (2024) are based on empirical metallicity calibrations that can be strongly affected by uncertainties in the ionization and temperature structure of the H II regions at high redshift. Larger samples of T_e -based metallicities at $z > 3$ will again be crucial in robustly characterizing the FMR evolution at the highest redshifts (e.g., Stasińska 2010; Patrício et al. 2016; Nakajima et al. 2022, 2023).

6.3. The Mass-Neon Relation (MNeR)

Since Ne has the same nucleosynthetic origins as O, the total Ne/H abundance also correlates with the stellar mass. In the bottom panel of Figure 7, we present the mass-neon relation (MNeR) for CLASSY. The solid line in Figure 7 represents the unweighted linear least-squares fit to the CLASSY data, and it is presented in the following expression:

$$12 + \log(\text{Ne}/\text{H}) = (5.93 \pm 0.33) + (0.18 \pm 0.04) \times \log M_*, \quad (8)$$

with a standard deviation of $\sigma = 0.22$ and $\log M_*$ in units of M_\odot . Note that we have omitted metal-rich galaxies with high values of Ne/O in CLASSY (see Figure 3). We have added the sample of $z > 4$ galaxies from Arellano-Córdova et al. (2022a), Isobe et al. (2023b), and Marques-Chaves et al. (2024) with direct T_e abundance determinations.

Table 4
The Mass and Abundance Pattern Relations of O, Ne, S, Cl, and Ar for CLASSY Galaxies

Ion (1)	α (2)	$12+\log(X/H)_0$ (3)	σ (4)
Ne	0.20 ± 0.04	5.93 ± 0.31	0.22
S	0.24 ± 0.04	4.32 ± 0.33	0.28
Cl	0.24 ± 0.09	2.47 ± 0.75	0.34
Ar	0.20 ± 0.03	3.97 ± 0.23	0.23

Note. α represents the slope, and $12+\log(X/H)$ is the total abundance of each element labeled in column (1). $12+\log(X/H) = \alpha M_* + 12+\log(X/H)_0$. σ represents the dispersion of the data with respect to the linear fit.

We measure the first MNeR at high redshift, finding an unweighted least-squares linear trend of

$$12 + \log(\text{Ne}/\text{H}) = (4.81 \pm 1.58) + (0.27 \pm 0.19) \times \log M_*, \quad (9)$$

with a standard deviation of $\sigma = 0.24$ and $\log M_*$ in units of M_\odot . We also provide in Table 4 the best fits to S, Cl, and Ar with respect to the stellar mass, showing similar slopes of ~ 0.20 – 0.24 (see Figure 10 in Appendix B).

The MNeR in Figure 7 suggests some evolution, but the lower Ne/H trend of the $z > 4$ galaxies are consistent within the MNeR uncertainties. The differences between $z > 7$ galaxies of Paper V (purple stars) and $z = 4$ – 8 galaxies of Isobe et al. (2023b, teal circles) might be due to the ICFs or the presence of a young population of massive stars (Isobe et al. 2023b). On the other hand, CEERS-1019 of Marques-Chaves et al. (2024) is in agreement with the sample of galaxies of Isobe et al. (2023b), showing a lower Ne/H abundance than the local SFGs. The dispersion in the high- z MNeR is comparable to what we find in CLASSY (see Table 4). Although this is the first assessment of the MNeR at high- z , robust measurements of Ne/H and Ne/O with T_e and a robust ICF are necessary to better interpret the shape of the MNeR and confirm or refute the lower values of Ne/O at $z > 6$.

7. Summary and Conclusions

We investigated the abundance patterns of Ne, S, Cl, and Ar using a sample of 43 SFGs from the CLASSY survey with significant T_e measurements. The CLASSY sample has enhanced SFRs compared to other local samples of SFGs, making it a useful reference sample for high-redshift galaxies. We used different sets of T_e -diagnostics to provide a robust characterization of the different ionization and temperature structures of the gas for each galaxy. Further, we analyzed a set of literature ICFs and determined the most appropriate ICFs for use with the CLASSY galaxies. The detailed inspection of the ICFs, T_e , and ionization structure of the CLASSY galaxies reduces biases related to the scatter and systematic trends with metallicity. As a result, we present robust measurements of abundance patterns of Ne/O, S/O, Cl/O, and Ar/O, and the total abundances of Ne, S, Cl, and Ar for CLASSY.

We examine the abundance patterns of CLASSY compared to two samples of local star-forming systems, (i) individual H II regions and (ii) integrated galaxies, to access the appropriateness of local calibrations for higher-redshift samples. We then compared to a high-redshift literature sample ($z > 3$) of abundances to investigate the chemical evolution of Ne, S,

Cl, and Ar. Finally, the broad galaxy properties covered in CLASSY (see Paper I and Paper IV) allow us to analyze essential scaling relations related to galaxy evolution. Our main conclusions can be summarized as follows:

1. With the accurate determination of the ionic abundances of the CLASSY galaxies, we carefully inspect the ICFs for Ne, S, Cl, and Ar. We find that the ICF for Ne of Dors et al. (2013) provides less scatter and an excellent agreement with the solar abundance. For the rest of the elements (S, Cl, and Ar), the ICFs of Izotov et al. (2006) show less dispersion in comparison with other sets of ICFs examined in this study (e.g., Thuan et al. 1995; Dors et al. 2016; Amayo et al. 2021). However, we emphasize that the application of these ICFs needs to be done with care since these ICFs are not representative of the integrated spectra of SFGs. However, the size of the ICF scatter is not enough to explain the unexpected trends that we are seeing as a function of metallicity, particularly at high metallicity (see Section 4.2).
2. We present the abundance patterns of Ne/O, S/O, Cl/O, and Ar/O in concert with O/H. We find that these abundance patterns show a constant behavior with metallicity as expected for nucleosynthesis at $\sim 7.0 < 12 + \log(\text{O}/\text{H}) < 8.5$. We confirm the high values of Ne/O at high O/H might be due to inaccurate ICFs (e.g., Izotov et al. 2006; Guseva et al. 2011; Amayo et al. 2021). For Ar/O, we find a significant trend with metallicity, which is not expected at $12 + \log(\text{O}/\text{H}) > 8.2$. It is possibly explained by the uncertain performance of the ICF of Ar at high metallicities, in particular, when [Ar III] line alone is used to calculate Ar/O.
3. We analyze the abundance trends of Ne/O, S/O, Cl/O, and Ar/O with respect to the relative abundances of Ne, S, Cl, and Ar. Here, we also confirm the trend at high metallicities as the Ne/H abundance increases. The explanation is still unclear, and a future exploration using chemical evolution models (Kobayashi et al. 2020a; Amayo et al. 2021; Alexander et al. 2023) is needed. In a similar way, the Ar/O versus Ar/H produces a significant trend as Ar/H increases, although the direction of this trend is opposite for CLASSY when compared to the sample of Miranda-Pérez & Hidalgo-Gómez (2023). Again, this suggests an important bias that might be related to the ICFs of Ar. Therefore, we stress the importance of revising the construction of the ICFs for all the elements, especially when they are applied to galaxies whose spectra are integrated.
4. We use the CLASSY abundance patterns as a reference to compare with the results of Ne, S, and Ar in $z > 4$ galaxies observed with the JWST. We carefully selected those galaxies with direct measurement of the metallicity using the T_e -sensitive method. We confirm that galaxies at $z > 7$ show similar values of Ne/O to $z \sim 0$ galaxies. However, a group of high- z galaxies show very low values of Ne/O (see also, Isobe et al. 2023b). For S/O and Ar/O, we selected galaxies where the ionic abundances were calculated using a fixed value of T_e and n_e . However, we stress that fixing a unique value of these two physical properties can result in a significant correlation with O/H (see Figure 6). Therefore, in this analysis, we confirm that there is no evolution of Ne/O,

S/O, and Ar/O across cosmic time and that S/O and Ar/O should be robustly evaluated in $z > 4$ SFGs.

5. The analysis of the MZR and FMR derived in CLASSY and $z > 4$ galaxies show no redshift evolution in terms of scatter. For the MZR, CLASSY galaxies show a steeper slope than those studied at high- z and a probable evolution at $z > 8$ (e.g., Nakajima et al. 2023). Note that we consider here those SFGs with abundance derived using the T_e -sensitive method. We present a new set of scaling relations based on CLASSY galaxies for Ne, S, Cl, and Ar (see Appendix B), which shows a slope similar to O, which is expected for the nucleosynthesis involved in those elements. We also report the MNeR for high- z galaxies, whose slope is steeper than the CLASSY galaxies and shifted to lower values of Ne.

Finally, the measurements of the physical conditions and chemical abundance of CLASSY allowed us to assess important biases involved in chemical abundance determinations of different elements. Therefore, CLASSY can be used as a reference to the abundance patterns of $z \sim 0$ and high- z SFGs. In particular, there are different JWST programs dedicated to the analysis of the chemical compositions of galaxies across cosmic time. These programs are focused on the detection of T_e -sensitive emission lines at $z \sim 3$ (CECILIA; Strom et al. 2023), Aurora (JWST program ID: 1914), and EXCELS (JWST program ID: 3543) at $z = 2-5$. In addition, this analysis will be useful for the upcoming observations of the Extremely Large Telescopes that will need robust abundance templates at $z \sim 0$ to trace and interpret the chemical enrichment of the Universe. We stress that the selection of ICFs plays an essential role in chemical abundance determinations of metals; however, much work remains to address the biases involved with the building of ICFs to correctly represent the broad range of conditions seen in SFGs. Our analysis with CLASSY provides a careful assessment of the abundance ratios of Ne, S, Cl, and Ar that can help to constrain the nucleosynthesis of chemical evolution models for a broad range of metallicities.

Acknowledgments

The CLASSY team thanks the referee for thoughtful feedback that improved this paper. We thank Chiaki Kobayashi for discussions on the chemical evolution of α -elements. K.Z. A.-C. and D.A.B. are grateful for the support for this program, HST-GO-15840, that was provided by NASA through a grant from the Space Telescope Science Institute, which is operated by the Associations of Universities for Research in Astronomy, Incorporated, under NASA contract NAS5-26555. The CLASSY collaboration extends special gratitude to the Lorentz Center for useful discussions during the ‘‘Characterizing Galaxies with Spectroscopy with a view for JWST’’ 2017 workshop that led to the formation of the CLASSY collaboration and survey. The CLASSY collaboration thanks the COS team for all their assistance and advice in the reduction of the COS data. K.Z.A.-C. and F.C. acknowledge support from a UKRI Frontier Research Guarantee Grant (PI Cullen; grant reference EP/X021025/1). B.L.J. and M.M. are thankful for support from the European Space Agency (ESA). J.B. acknowledges support by Fundação para a Ciência e a Tecnologia (FCT) through the research grants UIDB/04434/2020 and UIDP/04434/2020, through work contract No. 2020.03379.CEECIND, and through FCT project PTDC/

FISAST/4862/2020. R.A. acknowledges support from ANID Fondecyt Regular 1202007. This work also uses observations obtained with the large Binocular Telescope (LBT). The LBT is an international collaboration among institutions in the United States, Italy, and Germany. LBT Corporation partners are The University of Arizona on behalf of the Arizona Board of Regents; Istituto Nazionale di Astrofisica, Italy; LBT Beteiligungsgesellschaft, Germany, representing the Max-Planck Society, The Leibniz Institute for Astrophysics Potsdam, and Heidelberg University; The Ohio State University, University of Notre Dame, University of Minnesota, and University of Virginia.

Funding for SDSS-III has been provided by the Alfred P. Sloan Foundation, the Participating Institutions, the National Science Foundation, and the U.S. Department of Energy Office of Science.

The SDSS-III website is <http://www.sdss3.org/>. SDSS-III is managed by the Astrophysical Research Consortium for the Participating Institutions of the SDSS-III Collaboration including the University of Arizona, the Brazilian Participation Group, Brookhaven National Laboratory, Carnegie Mellon University, University of Florida, the French Participation Group, the German Participation Group, Harvard University, the Instituto de Astrofísica de Canarias, the Michigan State/Notre Dame/JINA Participation Group, Johns Hopkins University, Lawrence Berkeley National Laboratory, Max Planck Institute for Astrophysics, Max Planck Institute for Extraterrestrial Physics, New Mexico State University, New York University, Ohio State University, Pennsylvania State University, University of Portsmouth, Princeton University, the Spanish Participation Group, University of Tokyo, University of Utah, Vanderbilt University, University of Virginia, University of Washington, and Yale University.

This work also uses the services of the ESO Science Archive Facility, observations collected at the European Southern Observatory under ESO programs 096.B-0690, 0103.B-0531, 0103.D-0705, and 0104.D-0503.

Software: jupyter (Kluyver et al. 2016), astropy (Astropy Collaboration et al. 2018, 2022), PyNeb (Luridiana et al. 2015), LinRegConf (S. R. Flury 2024, in preparation; <https://github.com/sflury/LinRegConf>).

Appendix A Temperature Structure of CLASSY

In Figure 8, we present the temperature relations implied on the results of $T_e[\text{O II}]$, $T_e[\text{N II}]$, $T_e[\text{S III}]$, and $T_e[\text{O III}]$ for CLASSY color coded with the ionization parameter, $P = [\text{O III}] \lambda\lambda 4959, 5007 / ([\text{O II}] \lambda 3727 + [\text{O III}] \lambda\lambda 4959, 5007)$. For reference, the dashed line represents the one-to-one relation in each plot. The different lines in Figure 8 represent some common temperature relations used in the literature (e.g., Garnett 1992; Izotov et al. 2006). For a sample of 13 CLASSY galaxies, we analyze the $T_e[\text{N II}] - T_e[\text{O II}]$ relation (see panel (a) of Figure 8), which trace the low-ionization zone of the nebula. Some galaxies show significant departures to high values of $T_e[\text{N II}]$ (see Table 5). We have derived $T_e[\text{N II}]$ up to 6000 K larger than $T_e[\text{O II}]$, which is not expected if $T_e[\text{N II}]$ and $T_e[\text{O II}]$ trace similar gas conditions. For example, for J0036-3333, we measured $T_e[\text{N II}] = 27,200 \pm 100$ K, while a higher value was reported by Menacho et al. (2021, $T_e[\text{N II}] = 52,700$ K) for a similar region than in these observations. Another example is J0127-0619, with a value of $T_e[\text{N II}] = 30,400 \pm 2700$ (see

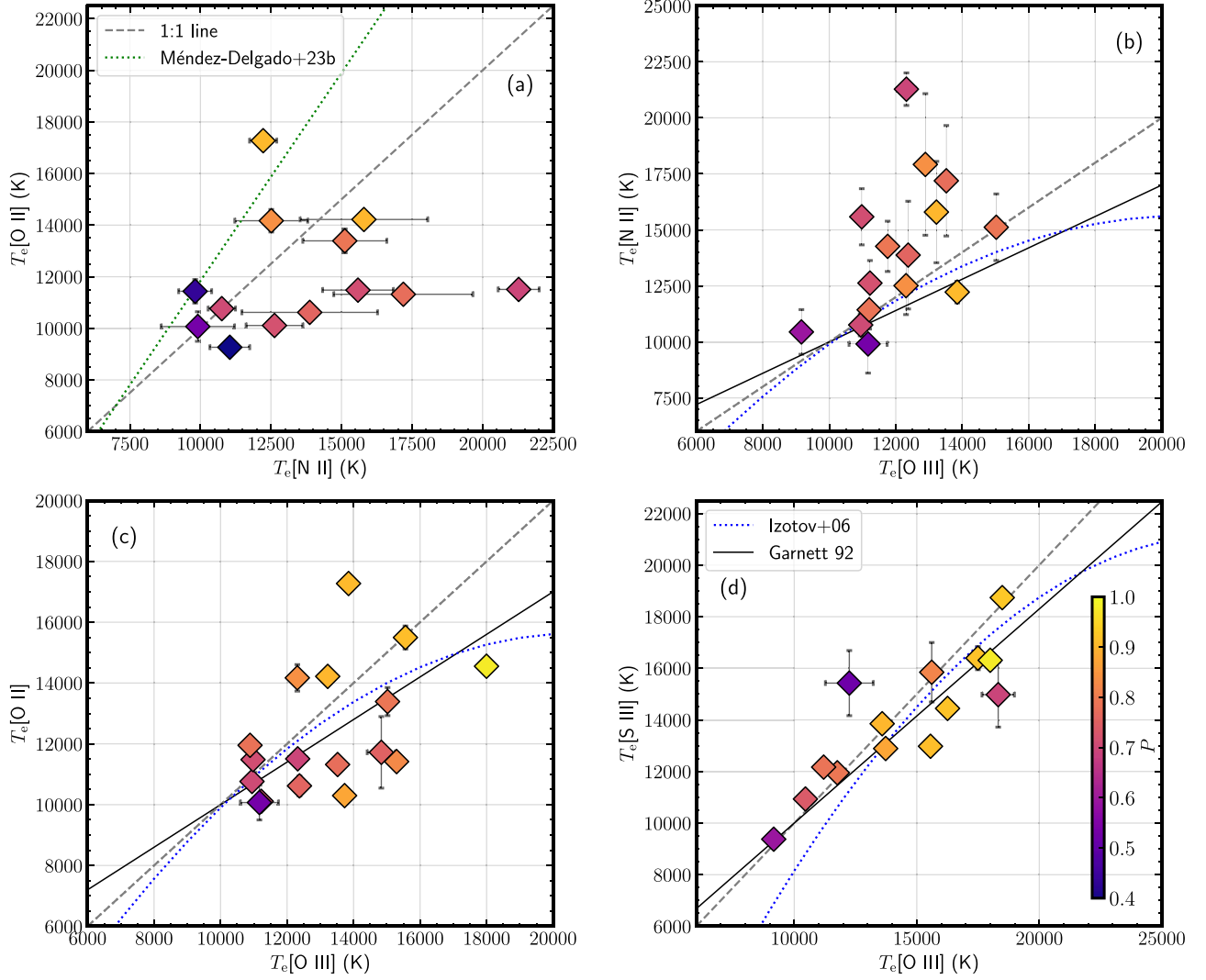


Figure 8. Temperature relations for the CLASSY sample as a function of the ionization parameter ($P = [\text{O III}] \lambda\lambda 4959,5007 / ([\text{O II}] \lambda 3727 + [\text{O III}] \lambda\lambda 4959,5007)$). Top: the low-ionization $T_e[\text{O II}] - T_e[\text{N II}]$ relation and the $T_e[\text{N II}] - T_e[\text{O III}]$ relation representative of the low and high ionization gas. Bottom: a comparison between the $T_e[\text{O II}] - T_e[\text{O III}]$ relation, and the intermediate and high ionization zones, $T_e[\text{S III}]$ and $T_e[\text{O III}]$. The temperature relations of Garnett (1992), Izotov et al. (2006), and Méndez-Delgado et al. (2023b) are represented in different lines and are labeled in each panel, respectively. While $T_e[\text{O II}]$ and $T_e[\text{S III}]$ as a function of $T_e[\text{O III}]$ follow the temperature relation from the literature, the $T_e[\text{N II}] - T_e[\text{O III}] / T_e[\text{O II}]$ relations show a large dispersion with a significant departure from those relations of the literature due to high values of $T_e[\text{N II}]$.

Table 5). This galaxy shows a broad component on the T_e -sensitive $[\text{N II}] \lambda 5755$ line, and the high value of $T_e[\text{N II}]$ could be related to the contribution of that component (see also James et al. 2009). However, we have used the fluxes related to the narrow component in our calculations (see also Paper IV).

One of the explanations for those high values in $T_e[\text{N II}]$ could be associated with the contribution by recombination. $[\text{N II}] \lambda 5755$ might be affected for the contribution of the recombination process of N^{2+}/H^+ (Rubin 1986) overestimating the value of $T_e[\text{N II}]$. Typically, to estimate the contribution by recombination to $[\text{N II}] \lambda 5755$, we use the expression derived by Liu et al. (2000), which depends on the measurement of N^{2+}/H^+ and can be estimated as $\text{N}^{2+}/\text{H}^+ = \text{N}/\text{H} - \text{N}^+/\text{H}^+$. Note that such an estimate is quite uncertain since it depends on the estimate of the N^{2+}/H^+ abundance. Menacho et al. (2021) also analyzed the contribution by recombination to the $[\text{N II}] \lambda 5755$ line (Liu et al. 2000; Stasińska 2005). Those authors found that this process is about 50%, which implies an overestimate of $T_e[\text{N II}]$. However, the

$[\text{O II}] \lambda\lambda 7220,30$ lines are even more affected by recombination; these authors found a minor contribution by this process to the emission of $[\text{O II}] \lambda\lambda 7220,30$ (less than 5%). Since both auroral lines should be affected in the same way, it is still uncertain as to what is driving the high values of $T_e[\text{N II}]$ (Loaiza-Agudelo et al. 2020; Menacho et al. 2021). In addition, in panel (a) of Figure 8, we have added the temperature relation of Méndez-Delgado et al. (2023b) based on a sample of H II regions, which shows a steeper relation in comparison to CLASSY and the 1:1 line. In general, our results of the $T_e[\text{O II}] - T_e[\text{N II}]$ relation are more consistent with a 1:1 line (see also Rogers et al. 2022).

Panels (b) and (c) of Figure 8 show the temperature relations of $T_e[\text{O III}]$ as a function of $T_e[\text{N II}]$ and $T_e[\text{O II}]$, respectively. We found a large discrepancy between $T_e[\text{N II}]$ versus $T_e[\text{O III}]$ due to the high values of $T_e[\text{N II}]$ for this sample. The dispersion in the $T_e[\text{N II}] - T_e[\text{O III}]$ relationship is discussed in previous studies, mainly for samples of H II regions (e.g., Pilyugin 2007; Croxall et al. 2016; Arellano-Córdova & Rodríguez 2020; Berg et al. 2020;

Rogers et al. 2021; Méndez-Delgado et al. 2023a). Although part of the dispersion might be real, these authors claim that part of such dispersion could be due to dependence on the ionization parameter (see Figure 8), the difference of the age of the stellar population, and observational problems such as the detection and measurement of faint T_e -sensitive lines.

For the $T_e[\text{O II}]$ versus $T_e[\text{O III}]$ relation, we found that SFGs with $P < 0.8$ follow the relations of Garnett (1992) and Izotov et al. (2006) for the range of temperatures associated with the CLASSY galaxies, while that of some galaxies with $P > 0.8$ departs to high values of $T_e[\text{O II}]$. Recently, Méndez-Delgado et al. (2023b) analyzed the density and temperature structure in H II regions, finding that the presence of high density clouds can have a direct impact on $T_e[\text{O II}]$ in comparison to $T_e[\text{N II}]$. For those galaxies in our sample with measurements of $T_e[\text{O II}]$ and $T_e[\text{N II}]$, we have recalculated O^+ to evaluate the impact of $T_e[\text{O II}]$ and $T_e[\text{N II}]$ on the total abundance of O. We can perform this exercise for 11 galaxies with measurements of $T_e[\text{O II}]$, $T_e[\text{N II}]$, and $T_e[\text{O III}]$. For these galaxies, we compare O/H implied by the contribution of O^+ by comparing the results of $T_e[\text{O II}]$ and $T_e[\text{N II}]$. We find that the differences in O/H are lower than 0.09 dex for most of the galaxies, while for four galaxies (J0021+0052, J1359+572, J1025+3622, J1025+3622, J1105+4444) the differences are in the range of 0.12–0.17 dex. In particular, for such galaxies, the values of $T_e[\text{N II}]$ are relatively high (see also Figure 8). As an alternative, we also analyzed the results implied using a temperature relation to estimate $T_e[\text{O II}]$ from $T_e[\text{O III}]$. Thus, we compare the differences in O/H derived using the temperature relation and the direct measurement of $T_e[\text{O II}]$. We found differences lower than 0.08 dex. Therefore, it is reasonable to use the direct measurement of $T_e[\text{O II}]$ to calculate O^+ for CLASSY.

In panel (c) of Figure 8, we show the $T_e[\text{S III}]$ versus $T_e[\text{O III}]$ relationship, which represents T_e associated with the intermediate and high ionization zones, $T_e(\text{Int.})$ and $T_e(\text{High})$, respectively. We find that most of the CLASSY galaxies follow the trend implied by the relation of Garnett (1992), as was reported previously in Paper IV and Paper V.

As a summary, from the different temperature diagnostics derived in CLASSY, we selected $T_e[\text{O II}]$ as the preferred $T_e(\text{Low})$ when $T_e[\text{O II}]$ is measured; otherwise, we use the value derived for $T_e[\text{N II}]$ with the exception of those galaxies with very high $T_e[\text{N II}]$. For such galaxies, we use as reference the measurement of $T_e[\text{S III}]$ or $T_e[\text{O III}]$ to estimate $T_e(\text{Low})$. For J0808+3948, we use $T_e[\text{N II}]$ as $T_e(\text{Low})$.

Appendix B Galaxy Property Correlations

For this section, we investigate any correlation between Ne/O, S/O, Cl/O, and Ar/O ratios (and Ne/H, S/H, Cl/H, Ar/H) and the galaxy properties such as the stellar mass, SFR, and EW(H β). We use the galaxy properties of CLASSY derived in Paper I. Figure 9 illustrates the comparison between Ne/O, S/O, Cl/O, and Ar/O and SFR (left), stellar mass (middle), and EW(H β) (right), respectively. In general, all the abundance ratios show a constant trend with all the galaxy properties. For Ne/O, there is a slight correlation between the SFR and the stellar mass as Ne/O increases. As we mentioned in Section 4.2.1, such a slight trend could be due to issues with the ICF of Ne. For Cl/O, the dispersion is larger than the rest of the elements showing a possible correlation with the stellar mass and EW(H β). One possibility to confirm or discard the trend of Cl/O with the galaxy properties is the detection of [Cl III] $\lambda\lambda 5518,31$ at higher metallicities or $\log(M_*/M_\odot) > 10$. However, [Cl III] $\lambda\lambda 5518,31$ are very faint making difficult the analysis of the Cl/O ratios. However, our results with CLASSY in comparison with H II regions with CHAOS suggest a possible correlation of Cl/O between metallicity and the stellar mass (see also Figure 3). In addition, Figure 10 shows the correlations between Ne/H, S/H, Cl/H, and Ar/H with respect to the SFR (left) and the stellar mass (right). Overall, such elements show a trend with those galaxy properties. Although for Cl, the dispersion is larger; it is also evident that there is a slight trend with SFR and the stellar mass. Also note the total abundance derived for each element depends on the measurement of O/H (e.g., $\text{Ne}/\text{H} = \text{Ne}/\text{O} \times \text{O}/\text{H}$). We have fitted a linear relation to the results of Figure 10, which are presented in Table 4. In general, we found slopes ranging from 0.20 to 0.24. The steeper slopes correspond to S and Cl, 0.24 ± 0.04 and 0.24 ± 0.09 , respectively. However, we calculated a large scatter of the fit with respect to the data of 0.34 for Cl. For Ne and Ar, we found similar values of the slope with a scatter of $\sigma \sim 0.20$ (see Table 4). Note that, for Ne, we discarded the galaxies with high values of Ne/O to the fit.

For the comparison with the SFR, the different abundance patterns show a large dispersion at low values of SFR < 0 and a constant behavior, while a tentative correlation with less scatter is more evident when the SFR increases for S and Ar. Although there is not a correlation between the EW(H β), Ne/H and S/H increase at fixed SFR in galaxies with low values of EW(H β). However, the large dispersion at lower values of Ne, S, and Ar is consistent with no correlation of these elements as SFR decreases.

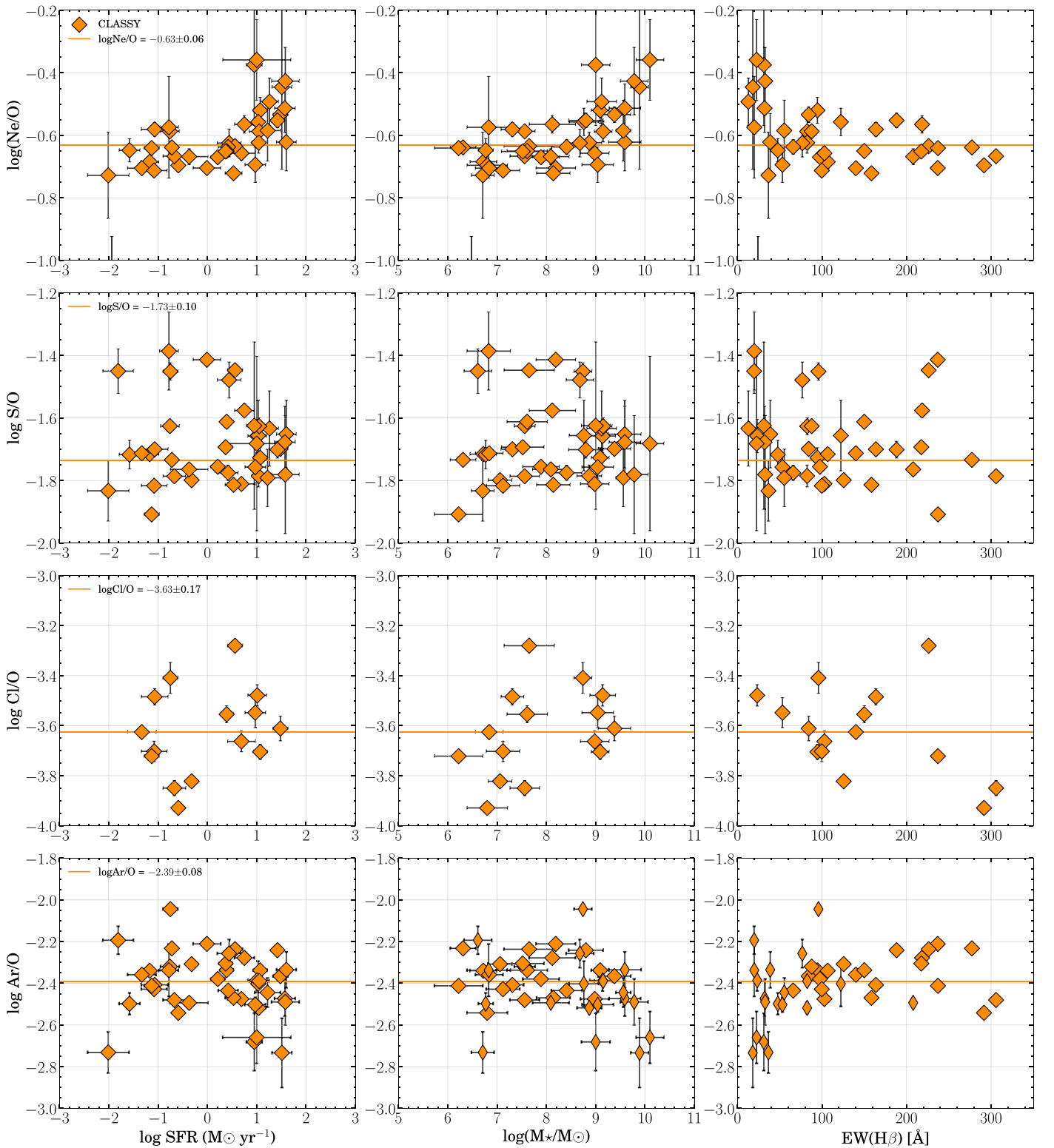


Figure 9. The abundance ratios of Ne/O, S/O, Cl/O, and Ar/O with respect to SFR (left), stellar mass (middle), and EW(H β) (right) for CLASSY. The orange line indicates the abundance ratio for CLASSY (see also Figure 3). The comparison of the abundance ratios derived in SFGs of the CLASSY sample shows a constant trend with the galaxy properties. The Cl/O abundance ratio shows a tentative correlation with stellar mass. A similar behavior is also shown in Figure 3 as a function of O/H.

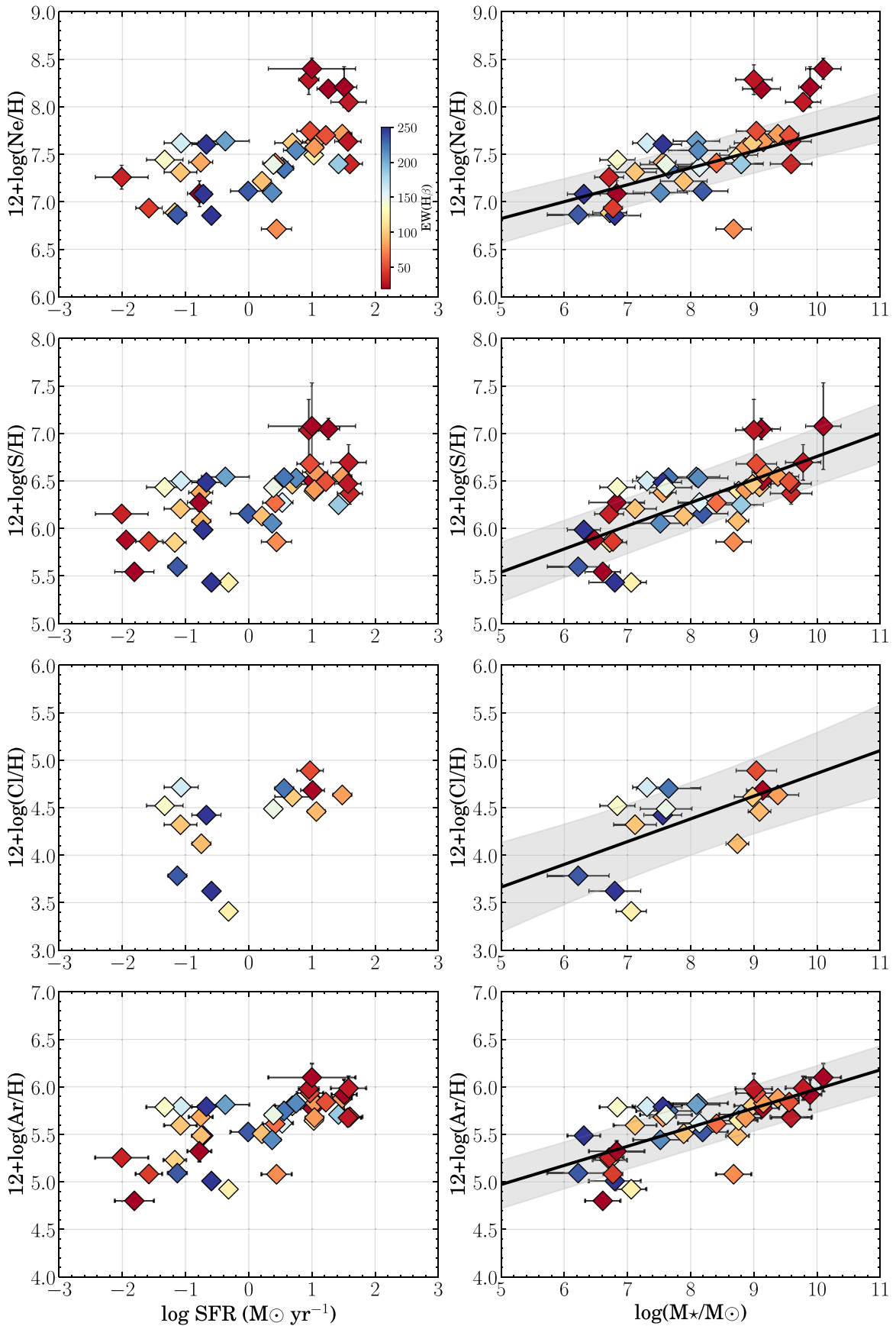


Figure 10. The total abundance ratios of Ne, S, Cl, and Ar with respect to SFR (left) and the stellar mass (right) for CLASSY in color coded with the EW of H β . Note that relation between Ne/H and MNeR is the same reported in Figure 7 for CLASSY. The solid lines show the best fit to the data with the stellar mass (see Appendix Table 6). The comparison with the SFR shows constant behaviors at $\log(\text{SFR}) < 0$. A tentative correlation of S/H and Ar/H with respect to SFR could be evident, but lower values of SFR show a large scatter as the abundance patterns decrease, showing no significant correlation with the SFR.

Appendix C

Tables: Physical Conditions, Chemical Abundances, and Galaxy Properties

In Table 5, we present the results of T_e and n_e for CLASSY, and the selected temperature structure in columns (7)–(9) to

determine the chemical abundances (see Section 3 and Appendix A). In Table 6, we list the stellar mass and SFR of CLASSY in columns (2)–(4). The metallicity, and the abundance ratios of Ne/O, S/O, and Cl/O and Ar/O are in columns (4)–(8).

Table 5
Electron Density and Temperature Structure of CLASSY

Galaxy	n_e [S II] (cm^{-3})	T_e [O II] (K)	T_e [N II] (K)	T_e [S III] (K)	T_e [O III] (K)	T_e (Low) (K)	T_e (Int.) (K)	T_e (High) (K)
(1)	(2)	(3)	(4)	(5)	(6)	(7)	(8)	(9)
J0021+0052	97 ± 32	11,500 ± 300	21,300 ± 800	...	12,300 ± 300	11,500 ± 300	11,900 ± 200	12,300 ± 300
J0036-3333	<100	...	27,200 ± 100	11,400 ± 100	...	10,600 ± 400	11,400 ± 900	11,700 ± 300
J0127-0619	408 ± 40	...	30,400 ± 2700	...	18,300 ± 400	15,800 ± 1700	16,900 ± 400	18,300 ± 400
J0337-0502	180 ± 10	20,200 ± 100	...	16,500 ± 600	20,200 ± 1500	22,200 ± 100
J0405-3648	28 ± 16	23,500 ± 1800	...	18,800 ± 1400	23,500 ± 2800	26,300 ± 100
J0808+3948	1179 ± 100	...	7500 ± 100	7500 ± 100	6900 ± 1000	6500 ± 100
J0823+2806	144 ± 24	10,800 ± 100	10,800 ± 500	...	10,900 ± 100	10,800 ± 100	10,800 ± 100	10,900 ± 100
J0926+4427	96 ± 70	11,700 ± 1100	14,800 ± 400	11,700 ± 1100	14,000 ± 400	14,800 ± 400
J0934+5514	<100	20,400 ± 200	17,300 ± 1800	18,600 ± 200	20,400 ± 200
J0938+5428	106 ± 37	11,500 ± 200	15,600 ± 1200	...	11,000 ± 200	11,500 ± 200	10,800 ± 200	11,000 ± 200
J0940+2935	9 ± 16	15,400 ± 1300	12,200 ± 1000	11,600 ± 1400	15,400 ± 1300	12,200 ± 1000
J0942+3547	50 ± 18	...	17,900 ± 3000	...	12,900 ± 100	12,000 ± 1300	12,400 ± 100	12,900 ± 100
J0944+3442	113 ± 48	15,300 ± 1600	13,700 ± 1800	14,400 ± 1300	15,300 ± 1600
J0944-0038	138 ± 56	15,500 ± 400	...	14,800 ± 500	15,600 ± 100	15,500 ± 400	14,800 ± 500	15,600 ± 100
J1016+3754	36 ± 25	16,400 ± 500	17,500 ± 200	15,200 ± 1600	16,400 ± 500	17,500 ± 200
J1024+0524	76 ± 19	11,400 ± 200	15,300 ± 100	11,400 ± 200	14,400 ± 100	15,300 ± 100
J1025+3622	198 ± 56	10,600 ± 300	13,900 ± 2600	...	12,400 ± 200	10,600 ± 300	12,000 ± 200	12,400 ± 200
J1044+0353	267 ± 19	23,400 ± 200	17,600 ± 200	15,300 ± 1600	23,400 ± 200	17,600 ± 200
J1105+4444	113 ± 23	10,100 ± 100	12,600 ± 1100	...	11,200 ± 100	10,100 ± 100	11,000 ± 100	11,200 ± 100
J1112+5503	408 ± 93	11,400 ± 400	9800 ± 600	11,400 ± 400	12,600 ± 1300	12,100 ± 100
J1119+5130	<100	15,800 ± 1100	15,600 ± 400	13,900 ± 1500	15,800 ± 1100	15,600 ± 400
J1129+2034	83 ± 15	10,900 ± 100	10,500 ± 100	10,300 ± 1200	10,900 ± 100	10,500 ± 100
J1132+1411	95 ± 24	12,000 ± 200	10,900 ± 100	12,000 ± 200	10,700 ± 100	10,900 ± 100
J1132+5722	122 ± 41	15,000 ± 1300	18,300 ± 600	15,800 ± 1700	15,000 ± 1300	18,300 ± 600
J1144+4012	109 ± 48	8600 ± 500	8600 ± 500	8500 ± 1200	8100 ± 600
J1148+2546	113 ± 10	10,300 ± 100	...	12,900 ± 100	13,700 ± 100	10,300 ± 100	12,900 ± 100	13,700 ± 100
J1150+1501	85 ± 12	...	14,300 ± 1200	12,000 ± 100	11,800 ± 100	11,200 ± 1200	12,000 ± 100	11,800 ± 100
J1157+3220	67 ± 15	...	10,400 ± 1000	9400 ± 200	9200 ± 200	9400 ± 1100	9400 ± 200	9200 ± 200
J1200+1343	172 ± 53	14,200 ± 400	12,500 ± 1200	...	12,300 ± 200	14,200 ± 400	11,900 ± 200	12,300 ± 200
J1225+6109	24 ± 19	13,900 ± 300	13,600 ± 100	12,500 ± 1400	13,900 ± 300	13,600 ± 100
J1253-0312	437 ± 35	17,300 ± 300	12,200 ± 500	...	13,800 ± 100	17,300 ± 300	13,200 ± 100	13,800 ± 100
J1314+3452	180 ± 15	...	11,400 ± 900	12,200 ± 100	11,200 ± 100	10,800 ± 1200	12,200 ± 100	11,200 ± 100
J1323-0132	629 ± 100	14,600 ± 300	...	16,300 ± 200	18,000 ± 100	14,600 ± 300	16,300 ± 200	18,000 ± 100
J1359+5726	69 ± 34	11,300 ± 200	17,200 ± 2600	...	13,500 ± 200	11,300 ± 200	12,900 ± 200	13,500 ± 200
J1416+1223	295 ± 61	10,700 ± 300	10,700 ± 300	11,500 ± 1200	11,000 ± 200
J1418+2102	73 ± 13	18,700 ± 100	18,500 ± 200	15,900 ± 1700	18,700 ± 100	18,500 ± 200
J1428+1653	119 ± 62	10,100 ± 500	9900 ± 1400	...	11,200 ± 600	10,100 ± 500	11,000 ± 500	11,200 ± 600
J1429+0643	63 ± 50	13,400 ± 500	15,100 ± 1500	...	15,000 ± 200	13,400 ± 500	14,200 ± 200	15,000 ± 200
J1448-0110	120 ± 29	14,200 ± 200	15,800 ± 2200	...	13,200 ± 100	14,200 ± 200	12,700 ± 100	13,200 ± 100
J1521+0759	76 ± 68	8900 ± 500	8900 ± 500	8900 ± 1200	8500 ± 100
J1525+0757	186 ± 60	8300 ± 200	8300 ± 200	8100 ± 1100	7600 ± 100
J1545+0858	153 ± 10	14,400 ± 100	16,300 ± 100	14,400 ± 1500	14,400 ± 100	16,300 ± 100
J1612+0817	484 ± 88	9300 ± 300	11,000 ± 700	9300 ± 300	9400 ± 1100	9000 ± 100

Note. Columns (7)–(9) show the low, intermediate, and high ionization T_e (low), T_e (Int), and T_e (low), respectively, used to calculate the ionic abundances; see Section 3.

Table 6
Galaxy Properties, Metallicity, and Chemical Abundance Ratios of Ne/O, S/O, Cl/O, and Ar/O of CLASSY







Galaxy (1)	z (2)	M_{star} (3)	$\log \text{SFR}$ (4)	$12+\log(\text{O}/\text{H})$ (5)	$\log(\text{Ne}/\text{O})$ (6)	$\log(\text{S}/\text{O})$ (7)	$\log(\text{Cl}/\text{O})$ (8)	$\log(\text{Ar}/\text{O})$ (9)
J0021+0052	0.0984	$9.09^{+0.18}_{-0.38}$	$1.07^{+0.14}_{-0.11}$	8.16 ± 0.17	-0.52 ± 0.03	-1.73 ± 0.03	-3.70 ± 0.03	-2.34 ± 0.03
J0036-3333	0.0206	$9.14^{+0.26}_{-0.23}$	$1.01^{+0.19}_{-0.21}$	8.16 ± 0.17	...	-1.66 ± 0.06	-3.48 ± 0.06	-2.39 ± 0.05
J0127-0619	0.0054	$8.74^{+0.18}_{-0.15}$	$-0.75^{+0.15}_{-0.13}$	7.53 ± 0.08	...	-1.45 ± 0.03	-3.41 ± 0.06	-2.04 ± 0.02
J0337-0502	0.0135	$7.06^{+0.24}_{-0.21}$	$-0.32^{+0.07}_{-0.11}$	7.23 ± 0.04	...	-1.80 ± 0.01	-3.82 ± 0.02	-2.31 ± 0.01
J0405-3648	0.0028	$6.61^{+0.28}_{-0.28}$	$-1.81^{+0.31}_{-0.27}$	6.99 ± 0.07	...	-1.45 ± 0.07	...	-2.19 ± 0.07
J0808+3948	0.0912	$9.12^{+0.30}_{-0.17}$	$1.26^{+0.18}_{-0.25}$	8.77 ± 0.05	-0.49 ± 0.05	-1.63 ± 0.12	...	-2.77 ± 0.14
J0823+2806	0.0472	$9.38^{+0.33}_{-0.19}$	$1.48^{+0.15}_{-0.32}$	8.25 ± 0.01	-0.53 ± 0.02	-1.70 ± 0.02	-3.61 ± 0.05	-2.37 ± 0.02
J0926+4427	0.1807	$8.76^{+0.30}_{-0.26}$	$1.03^{+0.13}_{-0.13}$	8.05 ± 0.09	-0.56 ± 0.12	-1.66 ± 0.12	...	-2.40 ± 0.12
J0934+5514	0.0025	$6.27^{+0.15}_{-0.20}$	$-1.52^{+0.09}_{-0.07}$	7.09 ± 0.01	-0.64 ± 0.01
J0938+5428	0.1021	$9.15^{+0.18}_{-0.29}$	$1.05^{+0.20}_{-0.17}$	8.22 ± 0.02	-0.59 ± 0.03	-1.63 ± 0.03	...	-2.39 ± 0.02
J0940+2935	0.0017	$6.71^{+0.23}_{-0.40}$	$-2.01^{+0.42}_{-0.37}$	7.99 ± 0.09	-0.73 ± 0.12	-1.83 ± 0.10	...	-2.73 ± 0.10
J0942+3547	0.0149	$7.56^{+0.21}_{-0.29}$	$-0.76^{+0.19}_{-0.12}$	8.00 ± 0.09	-0.59 ± 0.02	-1.63 ± 0.02	...	-2.32 ± 0.02
J0944+3442	0.0048	$6.83^{+0.44}_{-0.25}$	$-0.78^{+0.19}_{-0.16}$	7.66 ± 0.22	-0.57 ± 0.14	-1.39 ± 0.13	...	-2.34 ± 0.13
J0944-0038	0.0200	$8.19^{+0.40}_{-0.23}$	$-0.01^{+0.28}_{-0.65}$	7.82 ± 0.01	-0.70 ± 0.01	-1.66 ± 0.02	...	-2.29 ± 0.02
J1016+3754	0.0039	$6.72^{+0.27}_{-0.22}$	$-1.17^{+0.18}_{-0.18}$	7.57 ± 0.04	-0.68 ± 0.02	-1.72 ± 0.02	...	-2.34 ± 0.02
J1024+0524	0.0332	$7.89^{+0.37}_{-0.24}$	$0.21^{+0.14}_{-0.12}$	7.89 ± 0.01	-0.67 ± 0.01	-1.76 ± 0.02	...	-2.38 ± 0.02
J1025+3622	0.1265	$8.87^{+0.25}_{-0.27}$	$1.04^{+0.12}_{-0.18}$	8.19 ± 0.02	-0.62 ± 0.03	-1.79 ± 0.04	...	-2.52 ± 0.03
J1044+0353	0.0129	$6.80^{+0.41}_{-0.26}$	$-0.59^{+0.11}_{-0.14}$	7.55 ± 0.02	-0.70 ± 0.01	-2.12 ± 0.01	-3.93 ± 0.01	-2.54 ± 0.01
J1105+4444	0.0215	$8.98^{+0.29}_{-0.24}$	$0.69^{+0.28}_{-0.22}$	8.28 ± 0.01	-0.66 ± 0.02	-1.81 ± 0.02	-3.66 ± 0.04	-2.48 ± 0.02
J1112+5503	0.1316	$9.59^{+0.33}_{-0.19}$	$1.60^{+0.20}_{-0.25}$	8.02 ± 0.05	-0.62 ± 0.07	-1.65 ± 0.11	...	-2.34 ± 0.08
J1119+5130	0.0045	$6.77^{+0.15}_{-0.28}$	$-1.58^{+0.21}_{-0.12}$	7.58 ± 0.08	-0.65 ± 0.03	-1.72 ± 0.04	...	-2.50 ± 0.05
J1129+2034	0.0047	$8.09^{+0.37}_{-0.27}$	$-0.37^{+0.38}_{-0.56}$	8.31 ± 0.01	-0.67 ± 0.02	-1.76 ± 0.02	...	-2.49 ± 0.02
J1132+1411	0.0176	$7.31^{+0.23}_{-0.26}$	$-1.07^{+0.27}_{-0.35}$	8.20 ± 0.01	-0.58 ± 0.02	-1.70 ± 0.02	-3.48 ± 0.03	-2.41 ± 0.02
J1132+5722	0.0050	$8.68^{+0.28}_{-0.19}$	$0.44^{+0.24}_{-0.27}$	7.34 ± 0.02	-0.62 ± 0.04	-1.48 ± 0.06	...	-2.26 ± 0.06
J1144+4012	0.1269	$9.89^{+0.18}_{-0.29}$	$1.51^{+0.20}_{-0.29}$	8.65 ± 0.08	-0.45 ± 0.15	-2.73 ± 0.18
J1148+2546	0.0451	$8.14^{+0.34}_{-0.24}$	$0.53^{+0.17}_{-0.14}$	8.09 ± 0.02	-0.72 ± 0.01	-1.81 ± 0.01	...	-2.47 ± 0.01
J1150+1501	0.0024	$6.84^{+0.28}_{-0.30}$	$-1.33^{+0.29}_{-0.23}$	8.15 ± 0.02	-0.70 ± 0.01	-1.71 ± 0.01	-3.63 ± 0.02	-2.36 ± 0.01
J1157+3220	0.0110	$9.04^{+0.32}_{-0.18}$	$0.97^{+0.21}_{-0.42}$	8.44 ± 0.03	-0.69 ± 0.04	-1.76 ± 0.04	-3.55 ± 0.06	-2.50 ± 0.04
J1200+1343	0.0668	$8.12^{+0.47}_{-0.42}$	$0.75^{+0.20}_{-0.16}$	8.11 ± 0.01	-0.56 ± 0.03	-1.58 ± 0.02	...	-2.28 ± 0.02
J1225+6109	0.0023	$7.12^{+0.34}_{-0.24}$	$-1.08^{+0.26}_{-0.26}$	8.02 ± 0.06	-0.71 ± 0.01	-1.82 ± 0.01	-3.70 ± 0.04	-2.43 ± 0.02
J1253-0312	0.0227	$7.65^{+0.51}_{-0.23}$	$0.56^{+0.15}_{-0.15}$	7.98 ± 0.01	-0.63 ± 0.01	-1.45 ± 0.01	-3.28 ± 0.01	-2.24 ± 0.01
J1314+3452	0.0029	$7.56^{+0.30}_{-0.21}$	$-0.67^{+0.23}_{-0.55}$	8.27 ± 0.23	-0.67 ± 0.01	-1.79 ± 0.01	-3.85 ± 0.03	-2.48 ± 0.01
J1323-0132	0.0225	$6.31^{+0.26}_{-0.10}$	$-0.72^{+0.08}_{-0.09}$	7.72 ± 0.02	-0.64 ± 0.01	-1.73 ± 0.01	...	-2.23 ± 0.01
J1359+5726	0.0338	$8.41^{+0.31}_{-0.26}$	$0.42^{+0.20}_{-0.14}$	8.05 ± 0.01	-0.64 ± 0.02	-1.78 ± 0.02	...	-2.44 ± 0.02
J1416+1223	0.1232	$9.59^{+0.32}_{-0.26}$	$1.57^{+0.21}_{-0.25}$	8.15 ± 0.03	-0.51 ± 0.06	-1.68 ± 0.10	...	-2.47 ± 0.08
J1418+2102	0.0086	$6.22^{+0.49}_{-0.35}$	$-1.13^{+0.15}_{-0.16}$	7.50 ± 0.03	-0.64 ± 0.01	-1.91 ± 0.01	-3.72 ± 0.01	-2.41 ± 0.01
J1428+1653	0.1817	$9.56^{+0.15}_{-0.23}$	$1.22^{+0.26}_{-0.19}$	8.28 ± 0.07	-0.58 ± 0.08	-1.79 ± 0.09	...	-2.44 ± 0.08
J1429+0643	0.1735	$8.80^{+0.35}_{-0.21}$	$1.42^{+0.11}_{-0.17}$	7.95 ± 0.02	-0.55 ± 0.02	-1.70 ± 0.03	...	-2.24 ± 0.02
J1448-0110	0.0274	$7.61^{+0.41}_{-0.24}$	$0.39^{+0.13}_{-0.14}$	8.04 ± 0.02	-0.65 ± 0.02	-1.61 ± 0.01	-3.55 ± 0.03	-2.34 ± 0.01
J1521+0759	0.0943	$9.00^{+0.29}_{-0.30}$	$0.95^{+0.16}_{-0.17}$	8.66 ± 0.05	-0.37 ± 0.14	-1.62 ± 0.31	...	-2.68 ± 0.15
J1525+0757	0.0758	$10.10^{+0.28}_{-0.42}$	$1.00^{+0.69}_{-0.24}$	8.76 ± 0.05	-0.36 ± 0.08	-1.68 ± 0.31	...	-2.66 ± 0.14
J1545+0858	0.0377	$7.52^{+0.43}_{-0.26}$	$0.37^{+0.13}_{-0.17}$	7.75 ± 0.02	-0.65 ± 0.00	-1.69 ± 0.01	...	-2.31 ± 0.01
J1612+0817	0.1491	$9.78^{+0.28}_{-0.26}$	$1.58^{+0.28}_{-0.24}$	8.48 ± 0.19	-0.43 ± 0.06	-1.78 ± 0.21	...	-2.49 ± 0.10

Note. Columns (2)–(4): redshift, stellar mass, and SFR taken from Paper I, respectively. Column (5): metallicity. Columns (6)–(9): the Ne/O, S/O, Cl/O, and Ar/O abundance ratios.

ORCID iDs

Karla Z. Arellano-Córdova <https://orcid.org/0000-0002-2644-3518>
Danielle A. Berg <https://orcid.org/0000-0002-4153-053X>
Matilde Mingozzi <https://orcid.org/0000-0003-2589-762X>
Bethan L. James <https://orcid.org/0000-0003-4372-2006>
Noah S. J. Rogers <https://orcid.org/0000-0002-0361-8223>
Evan D. Skillman <https://orcid.org/0000-0003-0605-8732>
Fergus Cullen <https://orcid.org/0000-0002-3736-476X>

Ryan K. Alexander <https://orcid.org/0009-0006-2621-6979>
Ricardo O. Amorín <https://orcid.org/0000-0001-5758-1000>
John Chisholm <https://orcid.org/0000-0002-0302-2577>
Matthew Hayes <https://orcid.org/0000-0001-8587-218X>
Timothy Heckman <https://orcid.org/0000-0001-6670-6370>
Svea Hernandez <https://orcid.org/0000-0003-4857-8699>
Nimisha Kumari <https://orcid.org/0000-0002-5320-2568>
Claus Leitherer <https://orcid.org/0000-0003-2685-4488>
Crystal L. Martin <https://orcid.org/0000-0001-9189-7818>

Michael Maseda  <https://orcid.org/0000-0003-0695-4414>
 Themiya Nanayakkara  <https://orcid.org/0000-0003-2804-0648>
 Swara Ravindranath  <https://orcid.org/0000-0002-5269-6527>
 Allison L. Strom  <https://orcid.org/0000-0001-6369-1636>
 Fiorenzo Vincenzo  <https://orcid.org/0000-0002-0743-9994>
 Aida Wofford  <https://orcid.org/0000-0001-8289-3428>

References

- Aggarwal, K. M., & Keenan, F. P. 1999, *ApJS*, **123**, 311
 Alexander, R. K., Vincenzo, F., Ji, A. P., et al. 2023, *MNRAS*, **522**, 5415
 Amayo, A., Delgado-Inglada, G., & Stasińska, G. 2021, *MNRAS*, **505**, 2361
 Andrews, B. H., & Martini, P. 2013, *ApJ*, **765**, 140
 Arellano-Córdova, K. Z., Berg, D. A., Chisholm, J., et al. 2022a, *ApJL*, **940**, L23
 Arellano-Córdova, K. Z., Esteban, C., García-Rojas, J., & Méndez-Delgado, J. E. 2020, *MNRAS*, **496**, 1051
 Arellano-Córdova, K. Z., Esteban, C., García-Rojas, J., & Méndez-Delgado, J. E. 2021, *MNRAS*, **502**, 225
 Arellano-Córdova, K. Z., Mingozi, M., Berg, D. A., et al. 2022b, *ApJ*, **935**, 74
 Arellano-Córdova, K. Z., & Rodríguez, M. 2020, *MNRAS*, **497**, 672
 Arnaboldi, M., Bhattacharya, S., Gerhard, O., et al. 2022, *A&A*, **666**, A109
 Asplund, M., Amarsi, A. M., & Grevesse, N. 2021, *A&A*, **653**, A141
 Astropy Collaboration, Price-Whelan, A. M., Lim, P. L., et al. 2022, *ApJ*, **935**, 167
 Astropy Collaboration, Price-Whelan, A. M., Sipőcz, B. M., et al. 2018, *AJ*, **156**, 123
 Berg, D. A., Chisholm, J., Erb, D. K., et al. 2021, *ApJ*, **922**, 170
 Berg, D. A., Erb, D. K., Auger, M. W., Pettini, M., & Brammer, G. B. 2018, *ApJ*, **859**, 164
 Berg, D. A., Erb, D. K., Henry, R. B. C., Skillman, E. D., & McQuinn, K. B. W. 2019, *ApJ*, **874**, 93
 Berg, D. A., James, B. L., King, T., et al. 2022, *ApJS*, **261**, 31
 Berg, D. A., Pogge, R. W., Skillman, E. D., et al. 2020, *ApJ*, **893**, 96
 Berg, D. A., Skillman, E. D., Henry, R. B. C., Erb, D. K., & Carigi, L. 2016, *ApJ*, **827**, 126
 Berg, D. A., Skillman, E. D., Marble, A., et al. 2012, *ApJ*, **754**, 98
 Brinchmann, J. 2023, *MNRAS*, **525**, 2087
 Butler, K., & Zeppen, C. J. 1989, *A&A*, **208**, 337
 Cameron, A. J., Katz, H., & Rey, M. P. 2023b, *MNRAS*, **522**, L89
 Cameron, A. J., Katz, H., Rey, M. P., & Saxena, A. 2024a, *MNRAS*, **523**, 3616
 Citro, A., Berg, D. A., Erb, D. K., et al. 2024, *ApJ*, in press (arXiv:2305.14414)
 Clayton, D. 2003, *Handbook of Isotopes in the Cosmos* (Cambridge: Cambridge Univ. Press)
 Croxall, K. V., Pogge, R. W., Berg, D. A., Skillman, E. D., & Moustakas, J. 2016, *ApJ*, **830**, 4
 Curti, M., Cresci, G., Mannucci, F., et al. 2017, *MNRAS*, **465**, 1384
 Curti, M., D'Eugenio, F., Carniani, S., et al. 2023, *MNRAS*, **518**, 425
 Curti, M., Maiolino, R., Curtis-Lake, E., et al. 2024, *A&A*, **684**, A75
 De Robertis, M. M., Dufour, R. J., & Hunt, R. W. 1987, *JRASC*, **81**, 195
 Díaz, Á. I., & Zamora, S. 2022, *MNRAS*, **511**, 4377
 Domínguez-Guzmán, G., Rodríguez, M., Esteban, C., & García-Rojas, J. 2019, arXiv:1906.02102
 Domínguez-Guzmán, G., Rodríguez, M., García-Rojas, J., Esteban, C., & Toribio San Cipriano, L. 2022, *MNRAS*, **517**, 4497
 Dors, O. L., Hägele, G. F., Cardaci, M. V., et al. 2013, *MNRAS*, **432**, 2512
 Dors, O. L., Pérez-Montero, E., Hägele, G. F., Cardaci, M. V., & Krabbe, A. C. 2016, *MNRAS*, **456**, 4407
 Eisenstein, D. J., Johnson, B. D., Robertson, B., et al. 2024, *ApJS*, submitted (arXiv:2310.12340)
 Elia, D., Molinari, S., Schisano, E., et al. 2022, *ApJ*, **941**, 162
 Ellis, D. G., & Martinson, I. 1984, *PhyS*, **30**, 255
 Ellison, S. L., Patton, D. R., Simard, L., & McConnell, A. W. 2008, *ApJL*, **672**, L107
 Esteban, C., Bresolin, F., García-Rojas, J., & Toribio San Cipriano, L. 2020, *MNRAS*, **491**, 2137
 Esteban, C., García-Rojas, J., & Pérez-Mesa, V. 2015, *MNRAS*, **452**, 1553
 Finkelstein, S. L., Bagley, M. B., Ferguson, H. C., et al. 2023, *ApJL*, **946**, L13
 Fritzsche, S., Fricke, B., Geschke, D., Heitmann, A., & Sienkiewicz, J. E. 1999, *ApJ*, **518**, 994
 Froese Fischer, C., & Tachiev, G. 2004, *ADNDT*, **87**, 1
 Galavis, M. E., Mendoza, C., & Zeppen, C. J. 1995, *A&AS*, **111**, 347
 Garnett, D. R. 1990, *ApJ*, **363**, 142
 Garnett, D. R. 1992, *AJ*, **103**, 1330
 Grieve, M. F. R., Ramsbottom, C. A., Hudson, C. E., & Keenan, F. P. 2014, *ApJ*, **780**, 110
 Guseva, A. S., Pilyugin, L. S., Sakhibov, F., et al. 2012, *MNRAS*, **424**, 1930
 Guseva, N. G., Izotov, Y. I., Fricke, K. J., & Henkel, C. 2012, *A&A*, **541**, A115
 Guseva, N. G., Izotov, Y. I., Stasińska, G., et al. 2011, *A&A*, **529**, A149
 Henry, R. B. C., & Worthey, G. 1999, *PASP*, **111**, 919
 Isobe, Y., Ouchi, M., Nakajima, K., et al. 2023a, *ApJ*, **956**, 139
 Isobe, Y., Ouchi, M., Suzuki, A., et al. 2022, *ApJ*, **925**, 111
 Isobe, Y., Ouchi, M., Tominaga, N., et al. 2023b, *ApJ*, **959**, 100
 Izotov, Y. I., Guseva, N. G., Fricke, K. J., Henkel, C., & Schaerer, D. 2017, *MNRAS*, **467**, 4118
 Izotov, Y. I., Guseva, N. G., & Thuan, T. X. 2011, *ApJ*, **728**, 161
 Izotov, Y. I., Stasińska, G., Meynet, G., Guseva, N. G., & Thuan, T. X. 2006, *A&A*, **448**, 955
 Izotov, Y. I., Thuan, T. X., & Guseva, N. G. 2012, *A&A*, **546**, A122
 Izotov, Y. I., Thuan, T. X., & Guseva, N. G. 2021, *MNRAS*, **508**, 2556
 James, B. L., Berg, D. A., King, T., et al. 2022, *ApJS*, **262**, 37
 James, B. L., Tsamis, Y. G., Barlow, M. J., et al. 2009, *MNRAS*, **398**, 2
 Jones, T., Sanders, R., Chen, Y., et al. 2023, *ApJL*, **951**, L17
 Jones, T., Stark, D. P., & Ellis, R. S. 2012, *ApJ*, **751**, 51
 Kaufman, V., & Sugar, J. 1986, *JPCRD*, **15**, 321
 Kennicutt, R. C., Jr., Armus, L., Bendo, G., et al. 2003a, *PASP*, **115**, 928
 Kennicutt, R. C., Jr., Bresolin, F., & Garnett, D. R. 2003b, *ApJ*, **591**, 801
 Kewley, L. J., & Ellison, S. L. 2008, *ApJ*, **681**, 1183
 Kisielius, R., Storey, P. J., Ferland, G. J., & Keenan, F. P. 2009, *MNRAS*, **397**, 903
 Kluyver, T., Ragan-Kelley, B., Pérez, F., et al. 2016, in *Positioning and Power in Academic Publishing: Players, Agents and Agendas*, ed. F. Loizides & B. Schmidt (Clifton, VA: IOS Press), 87
 Kobayashi, C., Karakas, A. I., & Lugaro, M. 2020a, *ApJ*, **900**, 179
 Kobayashi, C., Leung, S.-C., & Nomoto, K. 2020b, *ApJ*, **895**, 138
 Kojima, T., Ouchi, M., Rauch, M., et al. 2021, *ApJ*, **913**, 22
 Kumari, N., James, B. L., Irwin, M. J., & Aloisi, A. 2019, *MNRAS*, **485**, 1103
 Kumari, N., Maiolino, R., Trussler, J., et al. 2021, *A&A*, **656**, A140
 Lara-López, M. A., Cepa, J., Bongiovanni, A., et al. 2010, *A&A*, **521**, L53
 Laseter, I. H., Maseda, M. V., Curti, M., et al. 2024, *A&A*, **681**, A70
 Leitherer, C., Schaerer, D., Goldader, J. D., et al. 1999, *ApJS*, **123**, 3
 Lequeux, J., Peimbert, M., Rayo, J. F., Serrano, A., & Torres-Peimbert, S. 1979, *A&A*, **80**, 155
 Li, M., Cai, Z., Bian, F., et al. 2023, *ApJL*, **955**, L18
 Licquia, T. C., & Newman, J. A. 2015, *ApJ*, **806**, 96
 Liu, X. W., Storey, P. J., Barlow, M. J., et al. 2000, *MNRAS*, **312**, 585
 Loaiza-Agudelo, M., Overzier, R. A., & Heckman, T. M. 2020, *ApJ*, **891**, 19
 Luridiana, V., Morisset, C., & Shaw, R. A. 2015, *A&A*, **573**, A42
 Maiolino, R., & Mannucci, F. 2019, *A&ARV*, **27**, 3
 Mannucci, F., Cresci, G., Maiolino, R., Marconi, A., & Gnerucci, A. 2010, *MNRAS*, **408**, 2115
 Marques-Chaves, R., Schaerer, D., Kuruvanthodi, A., et al. 2024, *A&A*, **681**, A30
 Matteucci, F., & Chiappini, C. 2005, *PASA*, **22**, 49
 McLaughlin, B. M., Lee, T.-G., Ludlow, J. A., et al. 2011, *JPhB*, **44**, 175206
 Menacho, V., Östlin, G., Bik, A., et al. 2021, *MNRAS*, **506**, 1777
 Méndez-Delgado, J. E., Esteban, C., García-Rojas, J., et al. 2023b, *MNRAS*, **523**, 2952
 Méndez-Delgado, J. E., Esteban, C., García-Rojas, J., Kreckel, K., & Peimbert, M. 2023a, *Natur*, **618**, 249
 Mendoza, C. 1983, in *IAU Symp. 103, Planetary Nebulae*, ed. L. H. Aller (Dordrecht: Reidel), 143
 Mendoza, C., & Zeppen, C. J. 1982a, *MNRAS*, **199**, 1025
 Mendoza, C., & Zeppen, C. J. 1982b, *MNRAS*, **198**, 127
 Mihalas, D. 1972, *Non-LTE Model Atmospheres for B and O Stars* (Boulder, CO: Natl. Cent. Atmos. Res.)
 Mingozi, M., James, B. L., Arellano-Córdova, K. Z., et al. 2024, *ApJ*, **962**, 95
 Miranda-Pérez, B. E., & Hidalgo-Gómez, A. M. 2023, *ApJ*, **952**, 76
 Mollá, M., García-Vargas, M. L., & Bressan, A. 2009, *MNRAS*, **398**, 451
 Morisset, C. 2009, *MmSAI*, **80**, 397
 Nakajima, K., Ouchi, M., Isobe, Y., et al. 2023, *ApJS*, **269**, 33
 Nakajima, K., Ouchi, M., Xu, Y., et al. 2022, *ApJS*, **262**, 3

- Osterbrock, D. E., & Ferland, G. J. 2006, *Astrophysics of Gaseous Nebulae and Active Galactic Nuclei* (2nd ed.; Sausalito, CA: Univ. Science Books)
- Patrício, V., Richard, J., Verhamme, A., et al. 2016, *MNRAS*, **456**, 4191
- Peimbert, M., & Costero, R. 1969, *BOTT*, **5**, 3
- Peimbert, M., Peimbert, A., & Delgado-Inglada, G. 2017, *PASP*, **129**, 082001
- Pérez-Montero, E., Hägele, G. F., Contini, T., & Díaz, Á. I. 2007, *MNRAS*, **381**, 125
- Pilyugin, L. S. 2007, *MNRAS*, **375**, 685
- Podobedova, L. I., Kelleher, D. E., & Wiese, W. L. 2009, *JPCRD*, **38**, 171
- Pontoppidan, K. M., Barrientes, J., Blome, C., et al. 2022, *ApJL*, **936**, L14
- Prantzos, N., Abia, C., Cristallo, S., Limongi, M., & Chieffi, A. 2020, *MNRAS*, **491**, 1832
- Ramsbottom, C. A., & Bell, K. L. 1997, *ADNDT*, **66**, 65
- Rhoads, J. E., Wold, I. G. B., Harish, S., et al. 2023, *ApJL*, **942**, L14
- Rogers, N. S. J., Skillman, E. D., Pogge, R. W., et al. 2021, *ApJ*, **915**, 21
- Rogers, N. S. J., Skillman, E. D., Pogge, R. W., et al. 2022, *ApJ*, **939**, 44
- Rogers, N. S. J., Strom, A. L., Rudie, G. C., et al. 2024, *ApJL*, **964**, 12
- Rubin, R. H. 1986, *ApJ*, **309**, 334
- Sanders, R. L., Shapley, A. E., Jones, T., et al. 2021, *ApJ*, **914**, 19
- Sanders, R. L., Shapley, A. E., Kriek, M., et al. 2016, *ApJ*, **816**, 23
- Schaerer, D., Marques-Chaves, R., Barrufet, L., et al. 2022, *A&A*, **665**, L4
- Stasińska, G. 2005, *A&A*, **434**, 507
- Stasińska, G. 2010, in *IAU Symp. 262, Stellar Populations—Planning for the Next Decade*, ed. G. R. Bruzual & S. Charlot (Cambridge: Cambridge Univ. Press), 93
- Stasińska, G., & Izotov, Y. 2003, *A&A*, **397**, 71
- Stephenson, M. G., Arellano-Córdova, K. Z., Berg, D. A., Mingozi, M., & James, B. L. 2023, *RNAAS*, **7**, 31
- Strom, A. L., Rudie, G. C., Trainor, R. F., et al. 2023, *ApJL*, **958**, L11
- Tayal, S. S. 2011, *ApJS*, **195**, 12
- Tayal, S. S., & Zatsarinny, O. 2010, *ApJS*, **188**, 32
- Thuan, T. X., & Izotov, Y. I. 2005, *ApJS*, **161**, 240
- Thuan, T. X., Izotov, Y. I., & Lipovetsky, V. A. 1995, *ApJ*, **445**, 108
- Torres-Peimbert, S., Peimbert, M., & Fierro, J. 1989, *ApJ*, **345**, 186
- Tremonti, C. A., Heckman, T. M., Kauffmann, G., et al. 2004, *ApJ*, **613**, 898
- Treu, T., Roberts-Borsani, G., Bradac, M., et al. 2022, *ApJ*, **935**, 110
- Trump, J. R., Arrabal Haro, P., Simons, R. C., et al. 2023, *ApJ*, **945**, 35
- Tumlinson, J., Peebles, M. S., & Werk, J. K. 2017, *ARA&A*, **55**, 389
- Vacca, W. D., Cushing, M. C., & Rayner, J. T. 2003, *PASP*, **115**, 389
- Vázquez, G. A., & Leitherer, C. 2005, *ApJ*, **621**, 695
- Watanabe, K., Ouchi, M., Nakajima, K., et al. 2024, *ApJ*, **962**, 50
- Williams, T. G., Gear, W. K., & Smith, M. W. L. 2018, *MNRAS*, **479**, 297
- Yang, H., Malhotra, S., Gronke, M., et al. 2017, *ApJ*, **844**, 171